CrossMark

Searching for Planets Orbiting Fomalhaut with JWST/NIRCam

Marie Ygouf[1] , Charles A. Beichman[1,2] , Jorge Llop-Sayson[1,3] , Geoffrey Bryden[1] , Jarron M. Leisenring[4] ,
András Gáspár[4] , John E. Krist[1], Marcia J. Rieke[4] , George H. Rieke[4] , Schuyler Grace Wolff[4] , Thomas L. Roellig[5] ,
Kate Su[4] , Kevin N. Hainline[4] , Klaus W. Hodapp[6] , Thomas P. Greene[5] , Michael R. Meyer[7] , Douglas M. Kelly[4],
Karl Misselt[4], John Stansberry[8] , Martha Boyer[8] , Doug Johnstone[9,10] , Scott Horner[5] , and Alexandra Z. Greenbaum[11]

[1] Jet Propulsion Laboratory, California Institute of Technology, Pasadena, CA 91109, USA; marie.ygouf@jpl.nasa.gov
[2] NASA Exoplanet Science Institute, IPAC, Pasadena, CA 91125, USA
[3] Department of Astronomy, California Institute of Technology, 1200 E. California Boulevard, Pasadena, CA 91125, USA
[4] Steward Observatory and the Department of Astronomy, The University of Arizona, 933 N Cherry Avenue, Tucson, AZ 85721, USA
[5] NASA Ames Research Center, Space Science and Astrobiology Division, MS 245-6, Moffett Field, CA 94035, USA
[6] University of Hawaii, Institute for Astronomy, 640 N. A'ohoku Place, Hilo, HI 96720, USA
[7] Department of Astronomy, University of Michigan, Ann Arbor, MI 48109, USA
[8] Space Telescope Science Institute, 3700 San Martin Drive, Baltimore, MD 21218, USA
[9] NRC Herzberg Astronomy and Astrophysics, 5071 West Saanich Road, Victoria, BC, V9E 2E7, Canada
[10] Department of Physics and Astronomy, University of Victoria, Victoria, BC, V8P 5C2, Canada
[11] IPAC, California Institute of Technology, 1200 E. California Boulevard, Pasadena, CA 91125, USA

Abstract

We report observations with the JWST/NIRCam coronagraph of the Fomalhaut (α PsA) system. This nearby A star hosts a complex debris disk system discovered by the IRAS satellite. Observations in F444W and F356W filters using the round 430R mask achieve a contrast ratio of $\sim 4 \times 10^{-7}$ at $1''$ and $\sim 4 \times 10^{-8}$ outside of $3''$. These observations reach a sensitivity limit of < 1 $M_{\rm Jup}$ across most of the disk region. Consistent with the hypothesis that Fomalhaut b is not a massive planet but is a dust cloud from a planetesimal collision, we do not detect it in either F356W or F444W (the latter band where a Jovian-sized planet should be bright). We have reliably detected 10 sources in and around Fomalhaut and its debris disk, all but one of which are coincident with Keck or Hubble Space Telescope sources seen in earlier coronagraphic imaging; we show them to be background objects, including the "Great Dust Cloud" identified in Mid-Infrared Instrument (MIRI) data. However, one of the objects, located at the edge of the inner dust disk seen in the MIRI images, has no obvious counterpart in imaging at earlier epochs and has a relatively red [F356W]–[F444W] > 0.7 mag (Vega) color. Whether this object is a background galaxy, brown dwarf, or a Jovian-mass planet in the Fomalhaut system will be determined by an approved Cycle 2 follow-up program. Finally, we set upper limits to any scattered light from the outer ring, placing a weak limit on the dust albedo at F356W and F444W.

Unified Astronomy Thesaurus concepts: Exoplanets (498); High contrast techniques (2369); Direct imaging (387); Coronagraphic imaging (313); Circumstellar disks (235); Infrared photometry (792); James Webb Space Telescope (2291); Infrared observatories (791); Space observatories (1543); Exoplanet detection methods (489); Exoplanet astronomy (486); Debris disks (363)

1. Introduction

At a distance of only 7.7 pc, the young ($\sim$500 Myr; Mamajek 2012; Nielsen et al. 2019) and bright ($V = 1.16$ mag) A3V star (Table 1), Fomalhaut (α PsA, HR 8728) was one of the original debris disk systems discovered by the IRAS satellite through the strong infrared excess at wavelengths longward of 12 μm (Aumann 1985; Gillett 1985). The debris disk phenomenon was soon recognized as a remnant of the planet formation process (Wyatt 2008). When the natal cloud dissipates, in addition to young planets there can be zones where planets did not form and that are occupied by reservoirs of small solid bodies that collide and grind each other down into small dust grains a few 10–100 s of microns in size. These grains are heated by the star to emit prominently at mid- and far-infrared wavelengths. The grains are ultimately lost by the system via a number of mechanisms, slowly depleting the reservoir of solid material (Wyatt 2008).

Debris disks are common among main-sequence K- through A-stars (Su et al. 2006; Carpenter et al. 2009; Eiroa et al. 2013; Thureau et al. 2014). At 24 μm, the phenomenon persists for $\sim$500 Myr, after which it decays to much lower levels (Rieke et al. 2005; Gáspár et al. 2013). The far-infrared emission persists for much longer, to $\sim$4 Gyr (Sierchio et al. 2014). For main-sequence (FGK but excluding late K) stars the fractional incidence of detectable cold debris disks is independent of the spectral type, roughly 20% at current sensitivity levels (Sierchio et al. 2014).

Only a few stars are close enough and have bright enough debris systems so that their disks can be resolved at wavelengths from the submillimeter to the visible, typically revealing material distributed in one or more narrow (few AU) rings separated by some 10 s of au. Fomalhaut is prominent among these. Imaging with the Hubble Space Telescope (Kalas et al. 2005; Gáspár & Rieke 2020) combined with infrared observations with Spitzer, Herschel (Stapelfeldt et al. 2004; Acke et al. 2012; Su et al. 2013), JWST (Gáspár et al. 2023),

Table 1
Properties of the Host Star Fomalhaut

Property	Value	Units	Comments
Spectral Type	A3 Va		Gray et al. (2006), Mamajek (2012)
T_{eff}	8590 ± 73	K	Mamajek (2012)
Mass	1.92 ± 0.02	$M_\odot$	Mamajek (2012)
Luminosity	16.6 ± 0.5	$L_\odot$	Mamajek (2012)
Age[a]	440	Myr	Mamajek (2012)
[Fe/H]	0.05 ± 0.04	dex	Gáspár et al. (2016)
R.A. (Eq 2000; Ep 2000)	$22^{\mathrm{h}}57^{\mathrm{m}}39\overset{s}{.}0$		van Leeuwen (2007)
Decl. (Eq 2000; Ep 2000)	$-29°37'20''\!.05$		van Leeuwen (2007)
Distance	7.70 ± 0.03	pc	van Leeuwen (2007)
Proper Motion (μ_α, μ_δ)	$(328.95, -164.67)$	mas yr^{-1}	van Leeuwen (2007)
V	1.155 ± 0.005	mag	Mermilliod & Mermilliod (1994)
J	1.054 ± 0.02	mag	Carter (1990)
H	1.010 ± 0.02	mag	Carter (1990)
K	0.999 ± 0.02	mag	Carter (1990)
L	0.975 ± 0.05	mag	Carter (1990)

Note.
[a] Nielsen et al. (2019) cite a slightly older age of 550 ± 70 Myr. For easier comparison with other analyses, we have adopted the 440 MYr age of Mamajek (2012).

and submillimeter observations from the James Clerk Maxwell Telescope (Holland et al. 2003) and Atacama Large Millimeter/submillimeter Array (ALMA; Boley et al. 2012; Su et al. 2016; MacGregor et al. 2017; White et al. 2017) have led to detailed understanding of the distribution of dust orbiting Fomalhaut. As shown by Gáspár et al. (2023), there is an outer "Kuiper Belt" ring at 140 au with $T \sim 50$ K, a second interior ring plus a broad distribution of heated dust extending inward toward the region thermally equivalent to the asteroid belt in the solar system. Fomalhaut also possesses a source of hot dust emission ($T \sim 1700$ K) seen via interferometry at ~ 2 μm that indicates the presence of hot dusty grains located within 6 au from Fomalhaut (Absil et al. 2009).

Multiple Hubble Space Telescope (HST) visits led to the detection of a co-moving source located interior of the ring—a candidate planet denoted Fomalhaut b (Kalas et al. 2008). Subsequent observations have called its planetary nature into question: the lack of infrared emission proportional to the visible brightness (Currie et al. 2013); a highly elliptical orbit projected to intersect the ring in a manner inconsistent with a stable planetary object (Beust et al. 2014); no evidence for Fomalhaut b was found in multiple epochs of Spitzer imaging (Marengo et al. 2009; Janson et al. 2015); and subsequent HST observations showing the object expanding in size and decreasing in brightness (Gáspár & Rieke 2020). The most likely explanation for the nature of Fomalhaut b is a slowly dissipating, expanding remnant of a collision of two planetesimals (Lawler et al. 2015; Gáspár & Rieke 2020).

No planets have as yet been detected within the Fomalhaut system. However, there are strong indications of unseen planets. Two have been invoked to shepherd the outer debris ring (e.g., Boley et al. 2012), while a third one is likely responsible for the configuration of the inner debris ring (Gáspár et al. 2023). Detection limits from observations of this system indicate that those planets are less massive than 3 M_{Jup} (Currie et al. 2013; Kenworthy et al. 2013; Janson et al. 2015). Theoretical estimates for the masses of the shepherding planets are smaller than these limits, $\leqslant 1$ M_{Saturn}.

In summary, Fomalhaut may host a complex planetary system, as reflected in its debris rings, the planetesimal collision that created Fomalhaut b, and the indications of unseen planets. Thus, it was with two goals in mind that we made Fomalhaut the target of a Guaranteed Time program with the James Webb Space Telescope (PID#1193) employing both the NIRCam and Mid-Infrared Instrument (MIRI): (1) search for planets within the Fomalhaut system at 3–5 μm, including a definitive measurement of Fomalhaut b; and (2) characterize the dust structures from 3 to 25 μm. This paper concentrates on the search for planets using NIRCam (Girard et al. 2022; Rieke et al. 2023). Gáspár et al. (2023) focus on the properties of the debris disk using MIRI (Wright et al. 2023).

2. NIRCam Observations

On 2022 October 22 we observed Fomalhaut at two roll angles in F444W and F356W filters using the round F430R mask with an inner working angle (IWA) of $\sim 0''\!.85$ (Krist et al. 2010). The exposure time at F444W was chosen to search for planets down to <1 M_{Jup} mass at $2''$ and beyond (~ 30 au) assuming a 5 nm wave-front drift and using representative models of the emission from young gas giants (Marley et al. 2021). The F356W observations were made to a depth adequate to identify and reject background stars or extragalactic objects based on their [F356W]–[F444W] color. The integration time in F356W was about a factor of 2 lower than at F444W to take advantage of the rising spectral energy distribution (SED) of stars to shorter wavelengths.

Those observations were obtained in two fields of view (FoV): with the SUB320 subarray ($20'' \times 20''$) selected to avoid saturation to search for companions as close to the star as possible, and in the full array ($2'\!.2 \times 2'\!.2$) mode to search for companions up to and beyond the outer ring, located at 140 au. The large FoV observations also have the potential to detect scattered emission from the outer ring, i.e., the near-IR counterpart of the ring seen by HST, depending on the properties of the dust grains.

We adopted the star δ Aqr (HR8709), an A3Vp star with $K_s = 3.06$ mag as a point-spread function (PSF) reference. The star is at a separation of $13°\!.8$ on the sky, but for the observing date in question, 2022 October 22, the change in solar illumination angle between the two stars is $\sim 7°\!.1$ which helps to minimize the thermal drift in the telescope (Perrin et al. 2018). We chose a $\sim 2\times$ longer exposure on the reference star to obtain a closer match of the signal-to-noise ratio (S/N) in the PSF for both targets. Table 2 describes the observing parameters for the deep imaging part of the NIRCam program. To account for the uncertainty in positioning the star in the center of the coronagraphic mask, we used the small-grid dithering (SGD) strategy (Lajoie et al. 2016) with the 5-POINT small (~ 10–20 mas) dither pattern on the reference star to increase the diversity in the PSF for post-processing and thus to increase the contrast gain at close separation. We maintained a similar S/N per frame for both targets by carefully choosing the detector readout modes, number of groups, and integrations.

Table 2
NIRCam Deep Imaging Observing Parameters (PID:#1193)

Target	Filter	Readout	Groups/Int	Ints/Exp	Dithers	Total Time (s)
Fomalhaut (Roll 1; Obs#14)	F356W/Mask 430R	FULL/RAPID	2	13	1	408
Fomalhaut (Roll 1; Obs#14)	F444W/Mask 430R	FULL/RAPID	2	24	1	762
Fomalhaut (Roll 1; Obs#15)	F356W/Mask 430R	SUB320/RAPID	3	105	1	451
Fomalhaut (Roll 1; Obs#15)	F444W/Mask 430R	SUB320/BRIGHT2	2	116	1	901
Fomalhaut (Roll 2; Obs#16)	F356W/Mask 430R	SUB320/RAPID	3	105	1	451
Fomalhaut (Roll 2; Obs#16)	F444W/Mask 430R	SUB320/BRIGHT2	2	116	1	901
Fomalhaut (Roll 2; Obs#17)	F356W/Mask 430R	FULL/RAPID	2	13	1	408
Fomalhaut (Roll 2; Obs#17)	F444W/Mask 430R	FULL/RAPID	2	24	1	762
HR8709 (Obs#18)	F356W/Mask 430R	SUB320/RAPID	9	17	5	910
HR8709 (Obs#18)	F444W/Mask 430R	SUB320/BRIGHT2	9	18	5	1830
HR8709 (Obs#19)	F356W/Mask 430R	FULL/RAPID	2	5	5	751
HR8709 (Obs#19)	F444W/Mask 430R	FULL/RAPID	3	7	5	1449

Note. The NIRCam program was executed on 2022-10-22 (2022.808).

3. Data Reduction and Post-processing

3.1. Pipeline Processing

The full set of images (summarized in Table 2) was processed using the JWST pipeline (version 2022_4a, calibration version jwst_1019.pmap). The data set can be obtained at:10.17909/kckm-n422. We started from the uncalibrated stage-1 data products as produced by the standard pipeline (Bushouse et al. 2023) with some modifications of the subsequent steps. Specifically, (1) we did not include dark current corrections, which are not well characterized for subarray observations; (2) we performed a modified version of the ramp fitting, as implemented within the SpaceKLIP package (Kammerer et al. 2022) to significantly improve the noise floor in the subarray images; and (3) to reduce saturation effects in the full array images, we allowed fluxes to be measured for ramps that only have a single group before saturation.

3.2. Bad Pixel Rejection and Horizontal Striping Removal

We performed additional steps to reject bad pixels and remove horizontal striping resulting from $1/f$ noise. The standard pipeline removes pixels adjacent to saturation-flagged pixels, which can result in an overly aggressive removal of good data. Since the images do not have any evidence of charge spillage, we utilized less conservative flagging (n_pix_grow_sat set to 0, rather than (1). For identification of truly bad pixels, we used the pipeline DQ flags: any pixels flagged as DO_NOT_USE, e.g., dead pixels, those without a linearity correction, etc., were set to NaN. 5σ outliers—temporally within subexposures or spatially within a 5×5 box—were also rejected.

After PSF subtraction, a set of additional bad pixels became apparent in the inner, speckle-dominated, region. The brightness of the speckles helps these bad pixels elude correction in the first steps of correction; we, thus, need to correct for these after PSF subtraction (Section 3.3). For the inner region ($\sim 3\rlap{.}''7 \times 3\rlap{.}''7$) of the PSF-subtracted non-coadded images, we apply a temporal and spatial bad pixel correction identical to the procedure described in the previous paragraph.

To remove horizontal striping resulting from $1/f$ noise, we subtracted the median value from each row of data (the direction of fast detector readouts). Figure 1 shows single F356W frames before and after horizontal stripe removal. Figure 2 shows the final coadded images in both F356W and F444W, prior to the next post-processing steps to remove residual starlight in the images.

3.3. Point-spread Function Subtraction

Following the basic data reduction for individual images, we combined the overall set of two roll angles on the primary target and a set of dithered observations of the reference star, using either reference star differential imaging (RDI) or angular difference imaging (ADI). We used two approaches for this post-processing—classical PSF subtraction and principal component analysis (PCA) taking advantage of the full diversity of the dithered reference PSFs. For the classical RDI, we first created a reference PSF from the nearby star HR8709, shifting and coadding its five dithered observations together to maximize S/N. We scaled and shifted the reference star PSF to align with the target at Roll 1 and Roll 2 independently before performing the PSF subtraction. For the classical ADI, we subtracted the two rolls from one another after applying the corresponding shift and data centering. In both RDI and ADI approaches, the last step after PSF subtraction was to orient both subtracted rolls to the North before coadding them resulting in a negative–positive–negative pattern for sources that are present in both telescope angles.

While the classical PSF subtraction performs well at larger distances from the target star where the noise is limited by the instrument sensitivity, at close separations residual starlight speckles are the dominant limitation to the detection of point sources. PCA analysis is preferred for cleaning the inner speckle field within $\sim 1\rlap{.}''5$. In this speckle-dominated region, we performed a PCA-based algorithm (Amara & Quanz 2012) via Karhunen Loéve Image Projection (KLIP; Soummer et al. 2012) using both the reference frames and the target frames from the opposite roll in the PSF library. We used the open-source Python package pyKLIP (Wang et al. 2015), which provides routines for cleaning the images, calculating detection limits, and quantifying the uncertainty in the flux of any detected sources.

The KLIP reduction was done using all available images (i.e., with six KL modes), with the full array mode data cropped
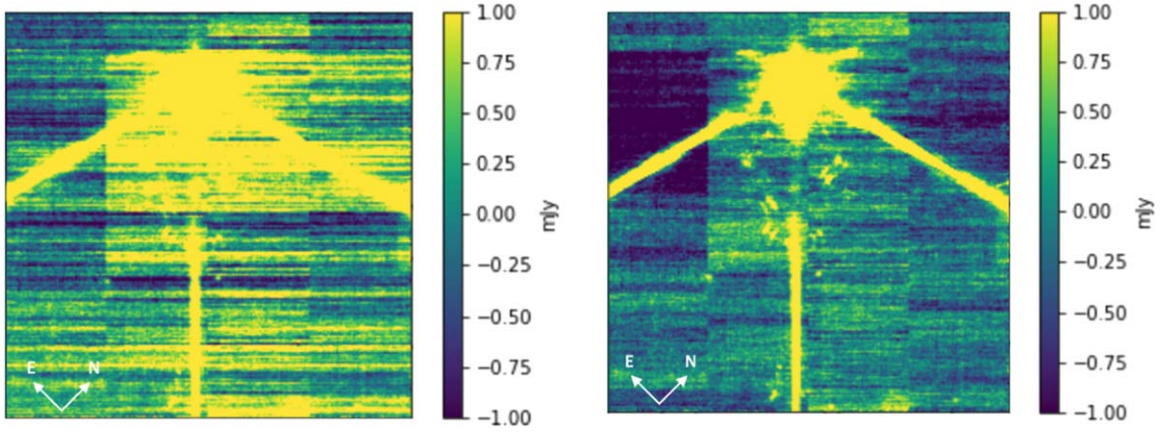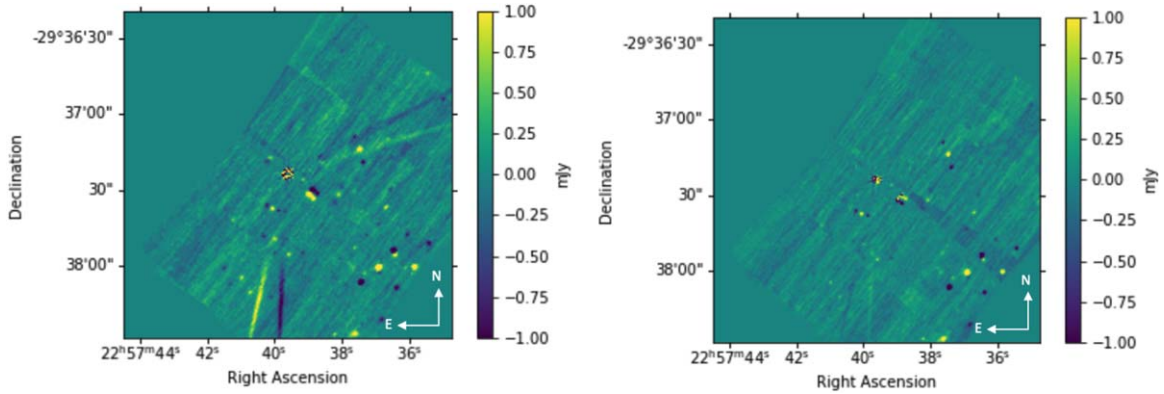
Figure 1. Single F356W full-frame images (2′.2 × 2′.2): raw (left) and corrected from horizontal stripes (right).
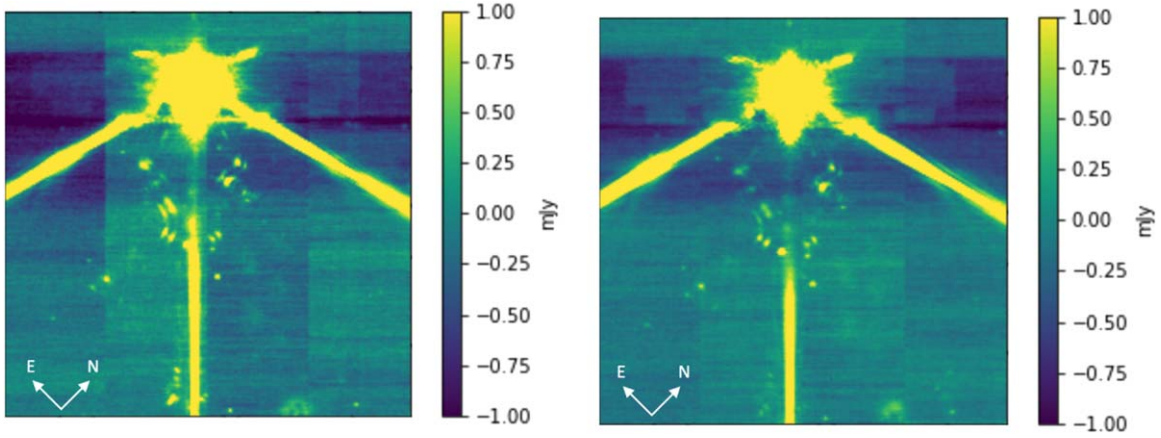
Figure 2. Coadded full-frame images (2′.2 × 2′.2) for F356W (left) and F444W (right) before post-processing to remove residual starlight.

Figure 3. Classical ADI reductions for the full-frame data sets for F356W (left) and F444W (right). The negative–positive–negative images surrounding each source are due to the subtraction of the two rolls as discussed in the text.

and centered to match the subarray mode data. Only the full array data set was used to produce the PCA full-frame reductions. The reference star data was used for PSF subtraction. Use of the 5-POINT-SMALL-GRID dither pattern mitigated any misalignment between the star and coronagraph focal plane mask.

Figures 3, 4, 5, and 6 show the results of the classical PSF and PCA subtractions. The presence of the expected negative–positive–negative image pattern is a good indication that a candidate object is real, even if its overall S/N is too low for

reliable extraction of its position and brightness. Sources S1-S10 discussed in Section 3.5 all show this pattern.

3.4. Contrast Calibration

The contrast limits reported in this work were obtained by normalizing the flux to a synthetic peak flux. Predicted fluxes in the JWST wave bands were calculated based on BOSZ stellar models (Bohlin et al. 2017) fit to optical and near-IR photometry (Table 1). Convolving the stellar model with JWST

4
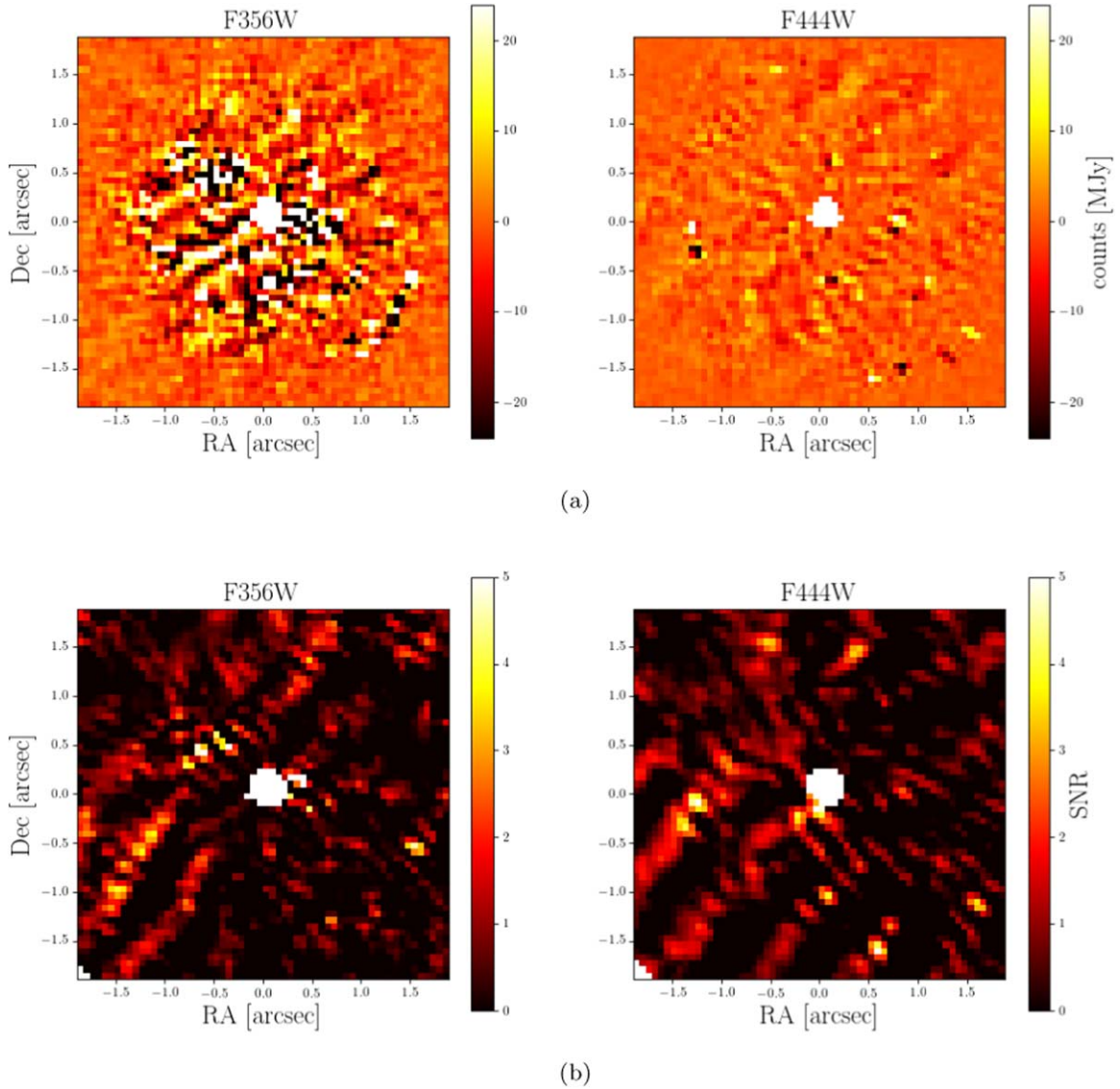
Figure 4. (Top) PCA reduction of the inner, speckle-dominated, region (inside ∼1″5). To emphasize the better results in the F444W filter, the images are displayed with the same absolute scale. The residual noise level is worse in the F356W image due to the brighter stellar flux and shorter integration time. (Bottom) S/N map from a forward model match filter (FMMF) analysis of the inner region of the Fomalhaut data. Pixels that yield an S/N of ∼5 are associated with residual bad pixels identifiable in the PSF-subtracted images and/or with residual instrument-related striping (diagonal structures going from the upper right to the lower left). There are no statistically significant peaks that could be ascribed to a planetary companion.

bandpasses gives an estimated flux of 115.6 Jy (0.93 mag) in the F356W filter and 80.9 Jy (0.89 mag) in F444W. To estimate the peak flux of the instrument's off-axis coronagraphic PSF we simulated this PSF using `WebbPSF` (Perrin et al. 2014). Measured fluxes in the NIRCam images were divided by these stellar fluxes to obtain contrast ratios. While the brightness of Fomalhaut often saturates CCD detectors at near-IR wavelengths (e.g., in the Two Micron All Sky Survey and Wide-field Infrared Survey Explorer all-sky surveys), Carter (1990) was able to use the 75-cm South African Astronomical Observatory to obtain JHK photometry with 2% accuracy (see Table 1), resulting in ∼2% overall uncertainty in our stellar flux estimates at JWST wavelengths; note that this uncertainty only contributes to the error budget for contrast ratios, not for the measured photometry that is used to calculate the contrast ratios.

The 3σ contrast curves (Figure 7(a)) were obtained using `pyKLIP`. While a 3σ threshold allows for the possibility of spurious detections, we find below that the overwhelming majority of sources above this threshold (all but one) are also detected by other telescopes, validating this threshold as appropriate for identifying potential sources for follow-up analysis. The noise was computed in an azimuthal annulus at each separation of the reduced image (before any smoothing), and we used a Gaussian cross correlation (kernel size = 2 pixels) to remove high-frequency noise. The contrast was calculated using the normalization peak value for the target star. We corrected for algorithmic throughput losses by injecting and retrieving fake sources at different separations. The contrast was also corrected for small sample statistics (Mawet et al. 2014) at the closest angular separations, although saturation is dominating around 1″ and below. At separations closer than 2″ the contrast is limited against the residuals from the PSF subtraction methods (∼4 × 10⁻⁷ at 1″, ∼1 × 10⁻⁷ at 2″), and further than 2″ the performance is limited by the background level (∼19 mag in F444W), consistent with the
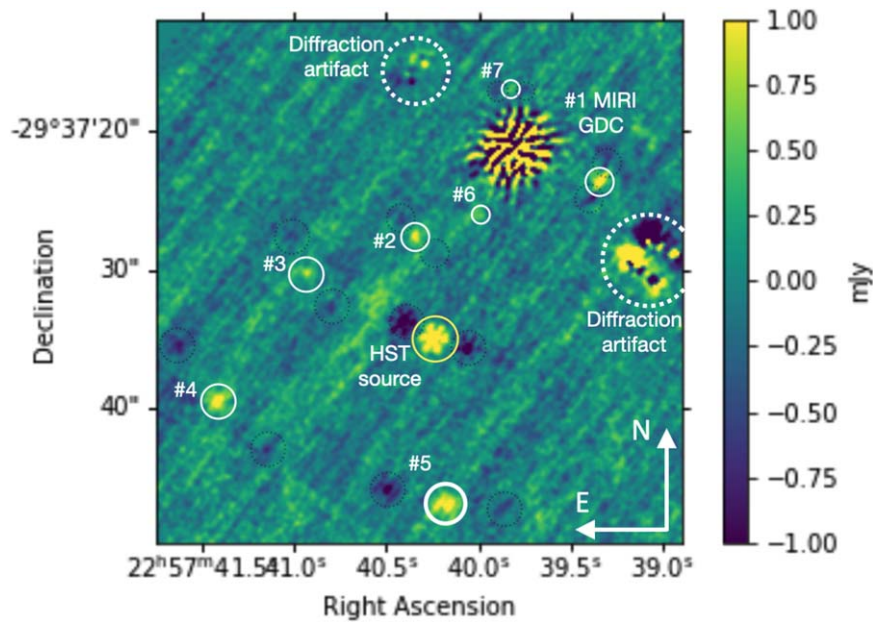
Figure 5. Zoomed-in F356W+F444W composite image highlighting the NIRCam sources (S1–S7 and one HST source (see Table 3 for details). The negative–positive–negative pattern reflects the effects of the roll subtraction. The image was Gaussian-filtered with a $\sigma = 2$ pixel kernel.

expectations of the instrument given the exposure time. Figure 7(b) converts the sensitivity curves into detection limits in Jupiter masses appropriate to Fomalhaut's age and distance ($<1\ M_{\rm Jup}$ beyond $2''$).

Losses due to the coronagraphic mask were taken into account in both the contrast curves and in the reported fluxes for any detected sources (the following section), although this is a negligible effect outside of $\sim 1''$. Transmission losses from the Lyot stop and coronagraph mask substrate were also included in both the contrast calibration and the point source photometry (Section 3.5 below). The mask substrate through-put is 0.95 and 0.93 for the F356W and F444W filters, while the transmission of the Lyot stop wedge is 0.98 in both.

3.5. Detection and Characterization of Point Sources near Fomalhaut

We adopted two methods to identify sources in the PSF-subtracted images, whether we considered the speckle-dominated or the outer region.

First, we focused on the inner, speckle-dominated region, looking for planet candidates within ($\sim 1.5''$; ~ 10–35 au) of Fomalhaut. Taking advantage of the telescope stability to generate a well-defined PSF, we applied a forward model match filter (FMMF; Ruffio et al. 2017) method. FMMF corrects for the KLIP's over-subtraction effects with a forward model (Pueyo 2016). This forward model was then used as a match filter to enhance the S/N of sources for which the spatial structure is well matched to the expected point source PSF. The PSF for the forward model was computed for each filter with WebbPSF using the OPD wave-front error map closest in time prior to the observations. No sources were reliably detected within this speckle-dominated region. The FMMF method is most useful for point source detection in the speckle-dominated region so we used a different method to identify sources in the outer region of the image.

Second, we visually examined the entire region interior and just the exterior of the debris ring, which has a radius of 140 au. Sources were initially detected using a Gaussian-smoothed image (kernel size = 2 pixels) to search for $>3\sigma$ candidates. These candidates were examined visually to identify stellar diffraction and other image artifacts.

The photometry and astrometry of the detected sources were recovered via a Markov Chain Monte Carlo (MCMC; emcee, Foreman-Mackey et al. 2013) fit to the PSF-subtracted data using pyKLIP. Sources for which the MCMC fit was unsatisfactory were analyzed with aperture photometry. For sources that manifest themselves differently from one method to another, the differences in the methodologies serve as a diagnostic for the source characteristics. Point sources, for example, will be detected more strongly with a method that matches the source to the predicted PSF like MCMC. Extended structures, on the other hand, will have poor fits to point source models.

Aperture photometry was performed with a $0\rlap{.}''25$ radius aperture (about 4 pixels) at the same location as the MCMC fit, with the background calculated within a 16 to 24 pixel annulus. While this aperture size is large relative to the nominal telescope resolution, diffraction by the coronagraphic mask and Lyot stop results in a much broader PSF, with a large fraction of the flux dispersed to wider angles; only 20%/25% of the flux is enclosed within the aperture for the F356W/F444W filters.

We simulated the coronagraphic PSF with WebbPSF_ext (J. Leisenring 2023 in preparation), deriving aperture corrections of 3.87 and 4.81 (multiplicative factors on the flux) for F356W and F444W, respectively, for our chosen aperture. We also measured the flux of each target within smaller and larger apertures (ranging from $0\rlap{.}''1$ to $1\rlap{.}''0$), finding that most of our sources yield consistent fluxes independent of aperture size (after applying the aperture correction), as expected for point sources. Some sources, however, have fluxes that rise significantly with aperture (e.g., S2 and S5), suggesting source
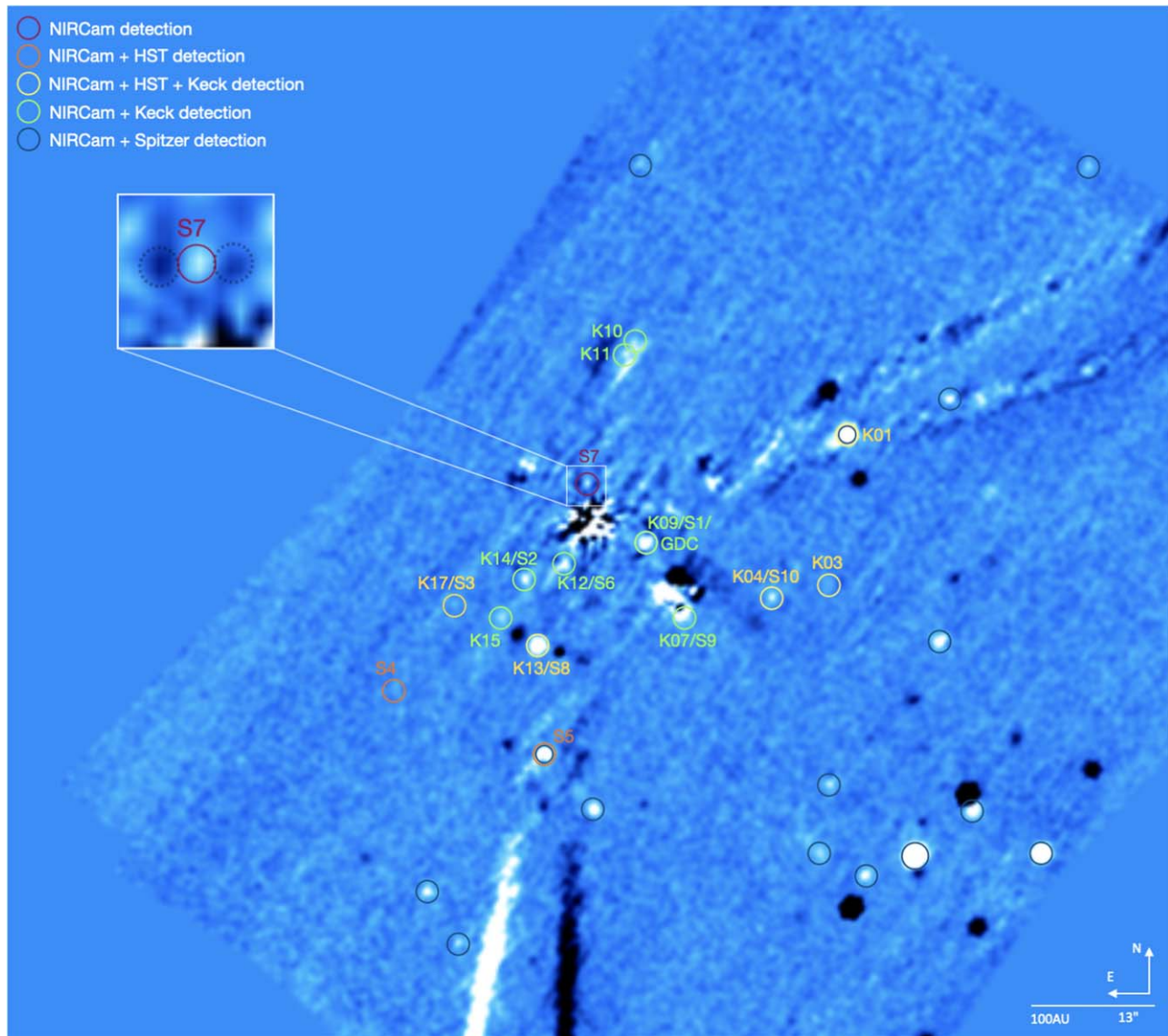
Figure 6. Combined F356+F444W full-frame classical ADI-reduced image showing some of the sources detected with NIRCam (labeled S1–S7) within and adjacent to the debris disk system. As discussed later in the text (Section 4) the figure also shows sources identified in Keck H-band imaging (Kennedy et al. 2023) obtained in 2005–2011 when Fomalhaut was ∼5″ from the position at which the NIRCam data were obtained (Epoch = 2022.808). Also shown are background sources detected with Spitzer 4.5 μm imaging from 2006.9 (Marengo et al. 2009).

sizes that are a fraction of an arcsecond. We determined the photometric uncertainty by placing the aperture at locations throughout the background annulus and measuring the dispersion in fluxes (again multiplied by the aperture correction factors). The standard aperture size (0.″25) was chosen to yield optimal S/N for point sources but also served adequately for the sources that are moderately extended. The measured fluxes and uncertainties are given in Table 3, with those determined via aperture photometry explicitly flagged. The calibration uncertainty for NIRCam (not included in the Table 3 uncertainties) is currently estimated as ∼5%,[12] much smaller than the photometric uncertainties for our low S/N detections.

Source positions were measured relative to Fomalhaut in the detector frame and converted to celestial coordinates using the star's position at the time of observation (including proper motion and parallax). As described in Greenbaum et al. (2023),

the position of the star in the detector was computed by performing cross-correlations of the data with synthetic PSFs, computed using `WebbPSF`. We use the `chi2_shift` functions in the `image-registration` Python package.[13] This method yields uncertainties of ∼7 mas, consistent with Carter et al. (2023).

We applied up to ∼30 mas distortion corrections to the WCS coordinate frame, based on a distortion map derived from on-sky observation of a dense stellar field (jwst_nircam_distortion_0173). The correction was performed with the `jwst` Calibration Pipeline (Bushouse et al. 2023). We estimated the astrometric accuracy to range from ∼10 mas for sources close to the central star up to ∼30 mas for sources outside of the Fomalhaut ring.

Images at F356W and F444W were treated separately, and the results are presented in Table 3. By design the integration

---
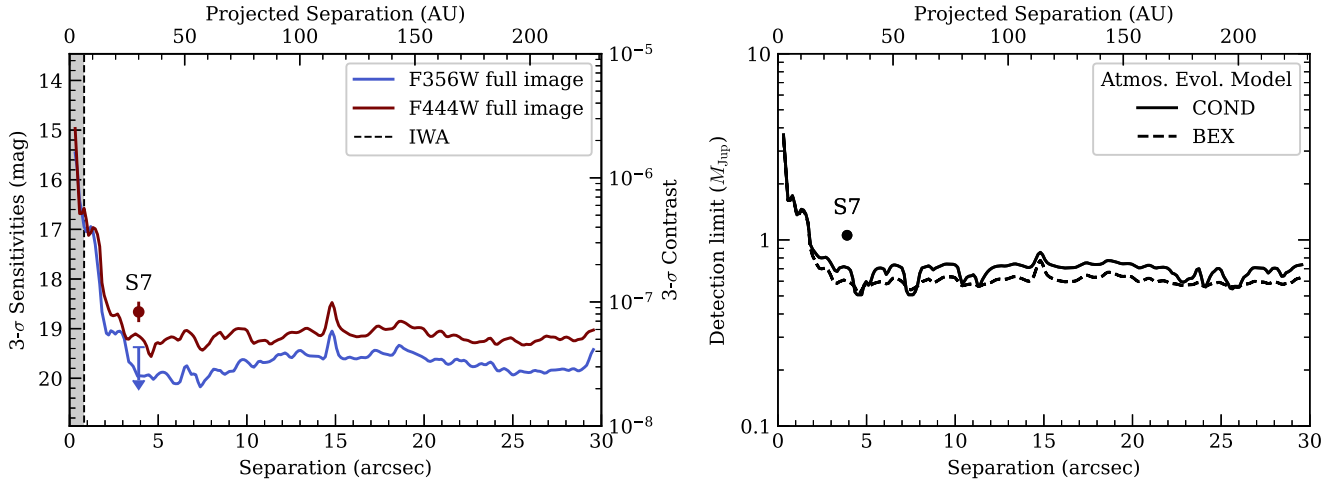
Figure 7. Coronagraphic full array observations of Fomalhaut with NIRCam achieve a 3σ sensitivity below 10^{-7} contrast at large separations from the star, limited primarily by the background and integration time. At an age of 440 Myr (Mamajek 2012), this contrast limit translates to a detection limit below 1 M_{Jup} outside of 2″, based on either AMES-Cond (Baraffe et al. 2003) or BEX-HELIOS (Linder et al. 2019) evolutionary models.

Table 3
Sources Detected by JWST/NIRCam

Source	Other Images[a]	$\Delta\alpha$ (″)	$\Delta\delta$ (″)	F356W Peak S/N[b]	(μJy)	(mag)	F444W Peak S/N	(μJy)	(mag)
S1	MIRI[c], K09	-6.10 ± 0.01	-2.28 ± 0.01	3.7	$6.84^{+0.54}_{-0.55}$	19.0 ± 0.12	3.7	$5.17^{+0.51}_{-0.47}$	18.9 ± 0.15
S2	K14	$+7.22 \pm 0.03$	-5.94 ± 0.04	3.3	$3.09^{+1.26}_{-1.42}$	19.8 ± 0.6	2.3	$1.24^{+1.11}_{-1.14}$	20.4 ± 0.7
S3[d]	MIRI,HST/STIS,K17	$+14.89 \pm 0.04$	-8.49 ± 0.06	3.4	5.08 ± 1.06	19.3 ± 0.2	3.8	3.39 ± 0.90	19.3 ± 0.3
S4[d]	MIRI, HST/WFC3	$+21.29 \pm 0.04$	-17.23 ± 0.04	4.2	2.94 ± 1.19	19.9 ± 0.4	4.1	3.02 ± 1.18	19.5 ± 0.4
S5[d]	HST/WFC3/Spitzer	$+4.69 \pm 0.01$	-25.31 ± 0.01	3.6	9.11 ± 0.94	18.7 ± 0.1	5.2	12.81 ± 0.69	17.9 ± 0.1
S6[d]	K12	$+2.80 \pm 0.03$	-4.59 ± 0.03	2.0	5.36 ± 1.00	19.3 ± 0.2	⋯	2.02 ± 1.00	19.9 ± 0.4
S7[d]	N/A	$+0.45 \pm 0.03$	$+3.91 \pm 0.03$	⋯	<4.26	>19.4	3.0	5.96 ± 1.13	18.7 ± 0.2
S8	HST/STIS,K13	$+5.77 \pm 0.003$	-13.29 ± 0.002	25.8	$56.22^{+2.01}_{-2.02}$	16.7 ± 0.07	26.7	$42.91^{+1.10}_{-1.14}$	16.6 ± 0.05
S9	HST/STIS,K07	-20.09 ± 0.013	-8.29 ± 0.011	6.0	$6.94^{+0.76}_{-0.80}$	19.0 ± 0.2	8.1	$5.86^{+0.63}_{-0.61}$	18.8 ± 0.2
S10	HST/STIS,K04	-28.21 ± 0.001	$+9.74 \pm 0.001$	31.7	$76.46^{+1.18}_{-1.16}$	16.4 ± 0.03	26.8	$64.01^{+0.85}_{-0.84}$	16.2 ± 0.02
Fomalhaut b[e]	HST	-9.377	11.144	⋯	<2.83	>19.4	⋯	<3.30	>19.4

Notes. The position offsets are relative to the current location of Fomalhaut (Epoch = 2022.808), located at $\alpha,\delta = 22^h57^m39^s\!.615, -29°37' 23''\!.87$, including the effects of proper motion and parallax. As denoted in Figure 8, the offsets in earlier HST epochs are consistent with the star's proper motion. Astrometric precision is based on the uncertainty in peak fitting; distortion contributes an additional systematic uncertainty of ~10–20 mas.

[a] Identification numbers for detected objects as seen in imaging by Keck (Kennedy et al. 2023), HST (Currie et al. 2013), and/or JWST/MIRI (Gáspár et al. 2023).

[b] The peak S/N is the S/N found by the initial peak finding routine (sensitive to single-pixel outliers), while the measured fluxes are based on either an MCMC-driven fit to the post-processed instrument PSF or, in the case of extended sources, from aperture photometry.

[c] The GDC source in the MIRI image is located at $\Delta\alpha, \Delta\delta = -6''\!.05 \pm 0''\!.3, -2''\!.42 \pm 0''\!.3$. The offset between MIRI's GDC and NIRCam's S1 is $-0''\!.05 \pm 0''\!.3, +0''\!.14 \pm 0''\!.3$.

[d] Flux densities and uncertainties for this source are derived from aperture photometry, rather than PSF fitting.

[e] Upper limit at the predicted position of Fomalhaut b, if it is on a bound orbit. A similar limit applies at the position of Fomalhaut b on an unbound orbit.

time in the shorter wavelength filter was smaller than at the longer wavelength, making the sensitivity at F356W worse than at F444W. The primary purpose of the F356W observation was the rejection of objects with typical stellar or galaxy-like SEDs.

We report in Table 3 the "peak S/N" associated with the brightest pixel of a given source. This is reported to quantify how much the source visually stands out over the noise. However, when extracting the photometry using the joint photometry and astrometry model fit, as explained above, the

error bars may differ from the peak S/N for lower signal detections. This discrepancy is due to the detections being excessively noisy due to bad pixels or poorly subtracted speckles. The figures in the Appendix show the model fit results of the data and model-selected point-like sources, e.g., S1, as well as the MCMC corner plots for the astrometric and photometric fits. The photometry and astrometry error bars provide the most complete accounting of the properties of the sources, whereas the peak S/N describes how well a source can be seen over the smoothed noise in the image.
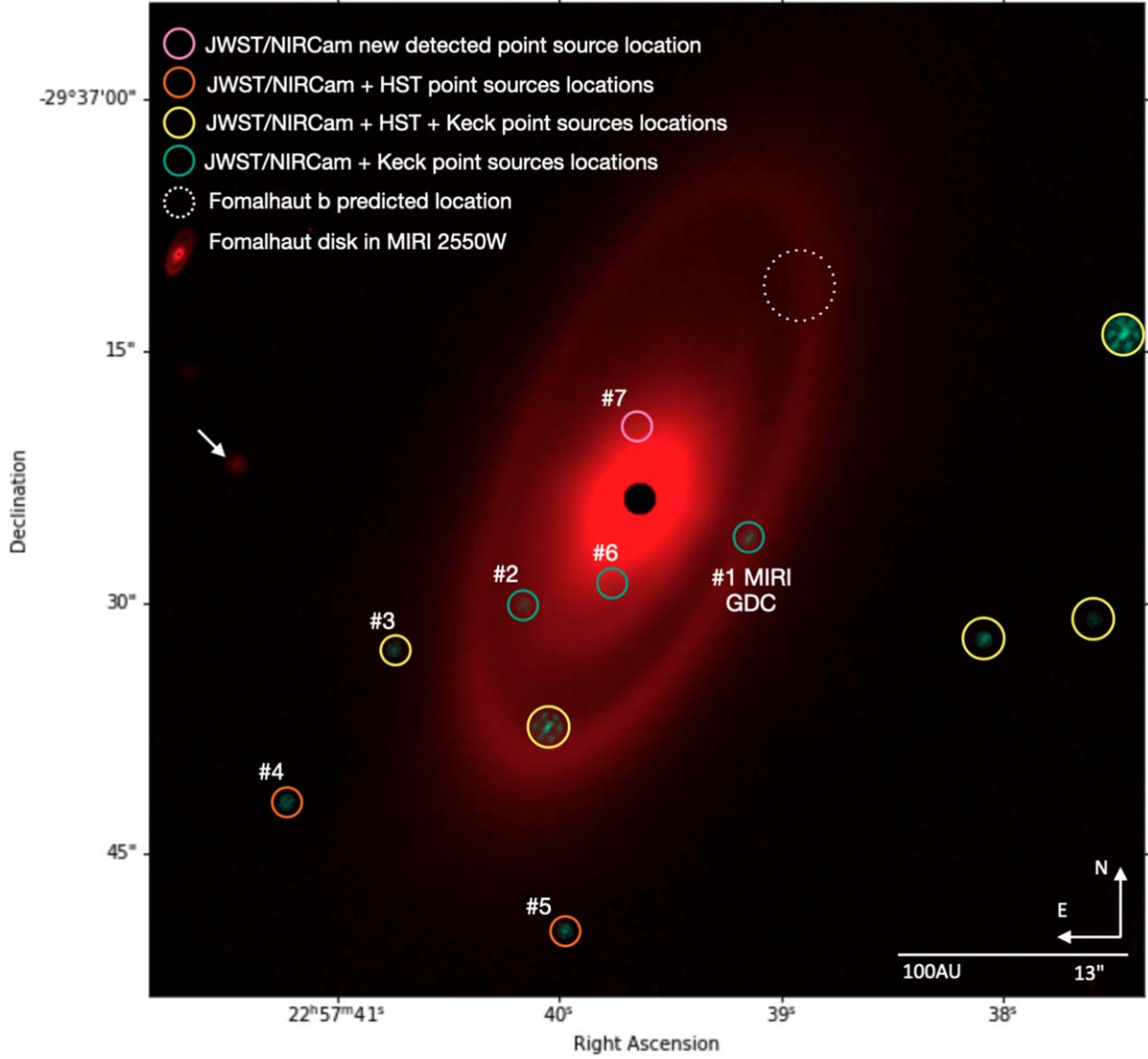
Figure 8. Point sources from the NIRCam/F356W+F444W image are shown with the MIRI F2550W PSF-subtracted image superimposed in red. Extracted NIRCam sources without HST counterparts are shown as green circles; NIRCam sources with HST-detected background objects (yellow); and instrument artifacts associated with the edge of the coronagraphic mask field of view (white). Source labels correspond to objects listed in Table 3. The red dotted circles denote the expected position of Fomalhaut b (Gáspár & Rieke 2020). No object is seen in this vicinity. We also note the presence of a bright MIRI point source at about 20″ East of Fomalhaut that does not have a NIRCam counterpart. The location of this point source, marked with a white arrow, coincides with the point source marked in Figure 6 of Janson et al. (2015).

4. Results

4.1. Sources in the Vicinity of Fomalhaut

Figure 4(a) shows the final images for the inner speckle field (<1″.5) around Fomalhaut. No sources are apparent, just a residual noise floor from imperfect speckle subtraction. Figure 4(b) shows the corresponding S/N map from the FMMF analysis of the inner region; applying an S/N = 5 threshold, the data yield no detections.

Figure 8 shows the sources extracted from the final NIRCam reduced image, along with a superposition of the MIRI data at F2300C. Some objects are clearly detected in Keck (circled in green), HST (circled in orange), or both HST and Keck (circled in yellow) images from earlier epochs.[14] One source, identified

with a white arrow in Figure 8, is visible in the MIRI data but has no counterpart in the NIRCam data. The location of this source coincides with the red point source identified in Spizter data from 2013 (see Figure 6 of Janson et al. 2015), indicating a background object. The source may be variable and not detectable at the NIRCam sensitivity levels, particularly at the very edge of the field of view. Alternatively, if the Spitzer object is not associated with the MIRI source and is indeed part of the Fomalhaut system, then the proper motion of Fomalhaut from 2013 to the present time would have resulted in the object falling very close to the edge of the field of view of the current NIRCam observations.

Table 3 summarizes the properties of the objects detected within 30″ of the star, corresponding to a projected separation of 230 au. Ten point sources are detected at either or both F356W and F444W with greater than 3σ significance. We have compared these sources against those detected in observations by Keck (Kennedy et al. 2023), HST (Currie et al. 2013), and

---

[14] See Table 1 of Gáspár & Rieke (2020) for a comprehensive list of HST observations of Fomalhaut, which include the Advanced Camera for Surveys (ACS) coronagraph in 2004 and 2006, and STIS in 2010 and 2014.
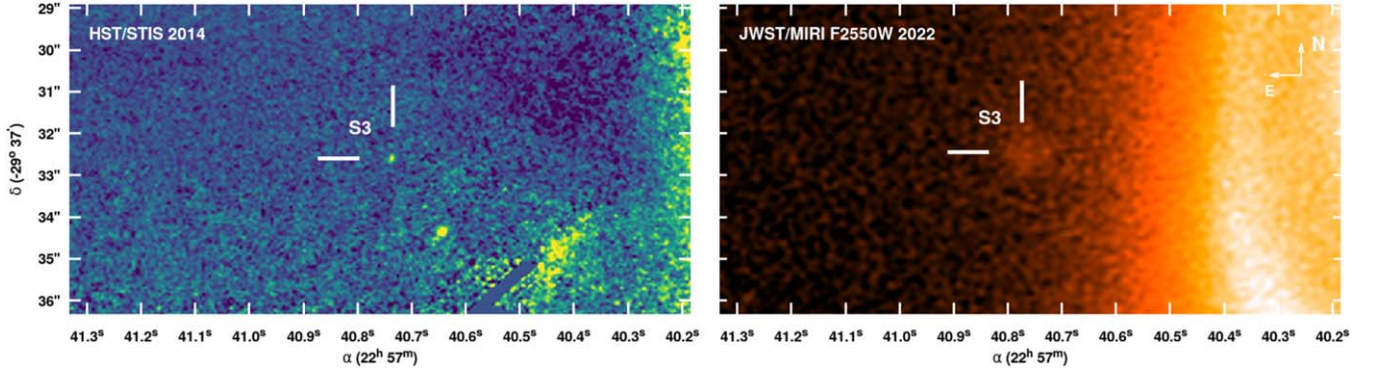
Figure 9. HST/STIS image from 2014 (left) and MIRI F2550W (right) showing the detection of S3 in both the HST and MIRI data. The source is detected at $\alpha = 22^h57^m40\overset{s}{.}73$, $\delta = -29°37'32\overset{''}{.}63$ in the HST/STIS image and offset by $0\overset{''}{.}39$ in the MIRI image at $\alpha = 22^h57^m40\overset{s}{.}76$, $\delta = -29°37'32\overset{''}{.}53$.
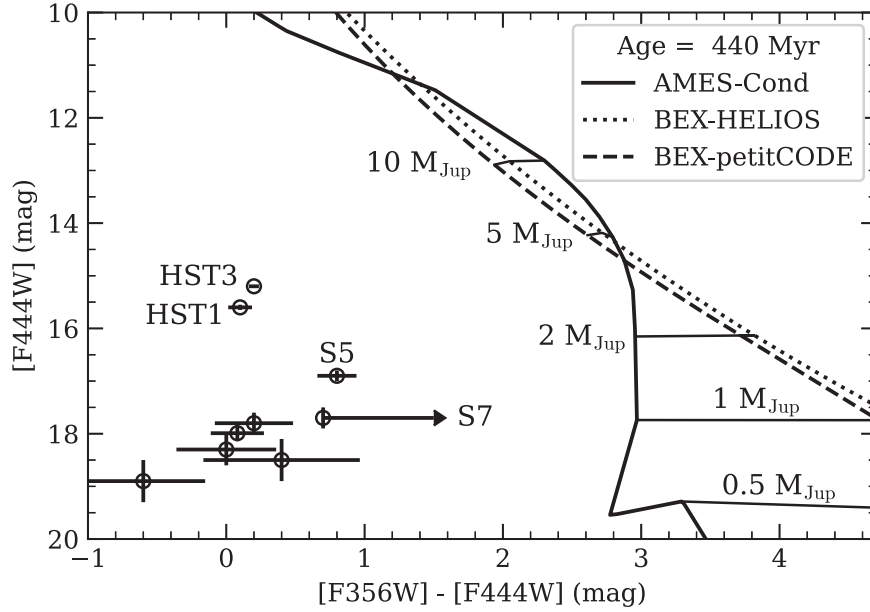
Figure 10. The F444W brightness and [F356W]−[F444W] color of our detected sources are compared against 440 Myr isochrones as a function of planet mass. Three evolutionary-radiative models are considered –AMES-Cond (solid line), BEX-HELIOS (dotted), and BEX-petitCODE with clouds (dashed). Masses from 0.5 to 10 M_{Jup} are marked on each isochrone. In the lower left-hand corner the source IDs are omitted for clarity, but from left to right are: S6, S3, S1, S9, and S4.

JWST/MIRI (Gáspár et al. 2023); all but one source—S7— have been previously imaged. We find that none of these previously identified sources are co-moving with Fomalhaut and we conclude that they are background objects.

A brief description of each source follows:

1. *S1*: The source sits within the combined NIRCam-MIRI positional uncertainties at the clump of emission seen in the MIRI coronagraphic image at 23.0 and 25.5 μm and denoted as the Great Dust Cloud (or GDC) by Gáspár et al. (2023). Detected at both F356W and F444W, it is separated from the GDC by $(\alpha, \delta) = (-50 \pm 300, +140 \pm 300)$ mas where the dominant source of uncertainty comes from the lower resolution MIRI image. The F356W/F444W color, [F356W]–[F444W] = 0.0 ± 0.2 Vega mag), is relatively blue (corresponding to a color temperature of $\sim 1700 \pm 400$ K). There is a Keck object, *K9*, as well as an ALMA source seen at this position confirming this as a background object (Kennedy et al. 2023). Astrometric coincidence within ~ 100 mas with Keck H-band objects from earlier epochs

(2005–2011) is used to identify S1 and all but one of the other NIRCam detections discussed below as background objects (Section 5). The F356W data for S1 show a hint of being extended, consistent with the galaxy interpretation (Figures 5, 12). As discussed further below (Section 5), comparing the combined NIRCam/MIRI spectral distribution with Spitzer SWIRE templates (Polletta et al. 2007) suggests that the object is an ultra-luminous IR galaxy like Arp 220 or M82 at a redshift $z = 0.8$–1.0

2. *S2*: This source is clearly detected at F356W with a peak S/N of 3.3 and marginally in F444W (Figure 13). Although S2 is positioned tantalizingly close to the outer edge of the innermost disk, close to the gap between the disk and the intermediate belt seen in the MIRI images (Gáspár et al. 2023), the presence of a Keck source at this position, *K14*, makes association with Fomalhaut improbable.

3. *S3 and S4*: These objects have high peak S/Ns in both F356W and F444W while the point source MCMC analysis provides a poor fit to the data. Aperture
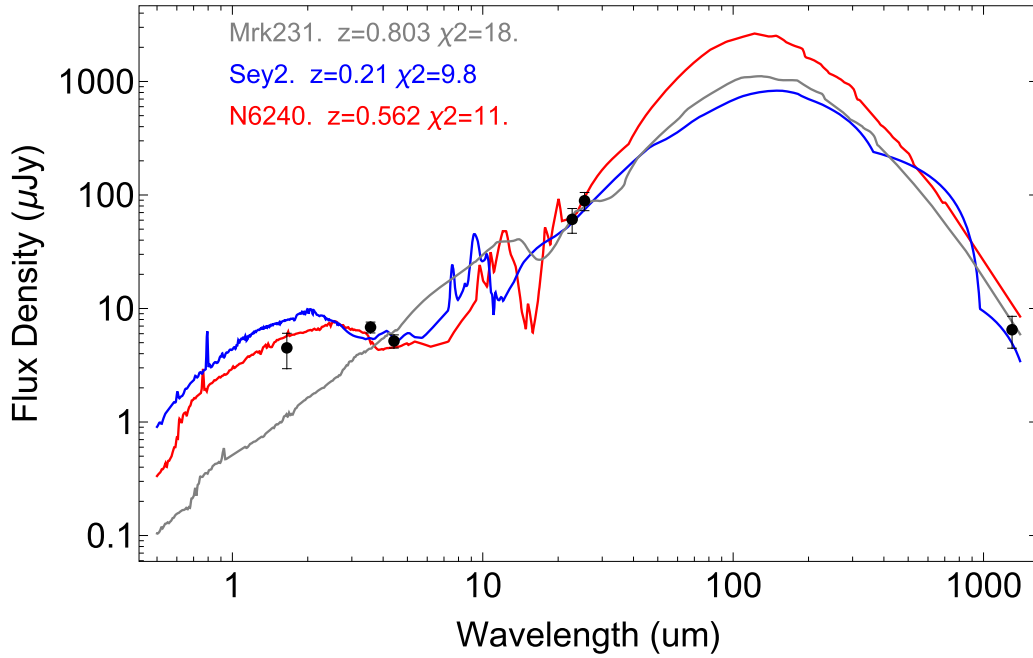
Figure 11. SED of S1 fitted to the model SEDs for three archetypal active galaxies, Markarian 231 (gray), average Seyfert 2 (blue), or NGC6240 (red) at redshifts of $z = (0.80, 0.21,$ and 0.56, respectively) using templates from the Spitzer SWIRE catalog (Polletta et al. 2007).

photometry of a slightly extended source ($\sim0\rlap.{''}25$–$0\rlap.{''}5$) provides robust photometric detections in both bands for both objects. S3 is detected in the Keck deep imaging, the 2014 HST/Space Telescope Imaging Spectrograph (STIS) image, and the MIRI data at F2550W (Gáspár et al. 2023 Figure 9). Although S4 is not seen in Keck imaging, it is detected by HST/WFC3 and its relatively blue color ([F356W]–[F444W] ~ 0 (Vega mag) is consistent with its being a distant galaxy. S4 is not seen in the F2550W imaging and falls outside the field of view of the F2300W data.

4. *S5*: This object sits well outside the Fomalhaut outer ring. It is robustly detected at both F356W and F444W. It is not seen in the Keck imaging and falls outside of the field of view of available HST data. Although the source is well fit with the PSF MCMC analysis (Figure 17), the aperture photometry finds increasing flux for larger apertures, suggesting an extended object. Although the [F356W]–[F444W] $= 0.8 \pm 0.2$ mag (Vega) color is more typical of a distant brown dwarf than a field galaxy (Section 5), the hint of extended emission suggests the latter interpretation.

5. *S6*: This object has marginal detections at F356W and F444W but is spatially coincident with an object seen in deep Keck imaging (*K12*). With [F356W]–[F444W] $= 0.6 \pm 0.4$ (Vega mag) it is likely to be a background galaxy.

6. *S7*: This object is a $\sim5\sigma$ detection at F444W and not detected at F356W, giving it a [F356W]–[F444W] color $\geqslant 0.7$ (Vega mag). It is without a Keck counterpart. If it were an exoplanet, it would have a mass of $\sim 1\ M_{\rm Jup}$ as suggested by Figure 10 and various models (Baraffe et al. 2003; Linder et al. 2019). What is most intriguing about this object, the only NIRCam object that cannot be immediately associated with a background source, is its proximity to the inner dust disk newly identified in the MIRI imaging (Gáspár et al. 2023, Figure 8). This disk

extends from $>1\rlap.{''}2$ outward to $10''$–$12''$, compared with the location of S7 at $4''$ (~30 au) separation from Fomalhaut. If associated with Fomalhaut and of the indicated mass, it should have substantial dynamical interactions with the inner debris disk, which are not evident in the 25.5 μm image. It will be important to address its possible effects on the structure of the inner disk if its planetary nature is confirmed.

7. *S8, S9, and S10*: These three objects are easily detected in both earlier HST/Keck imaging and the NIRCam data, making them obvious background objects. In particular, S10 looks extended in HST images.

Figure 10 compares the magnitudes and colors of our detected point sources. Most sources have $0 <$ [F356W]–[F444W] < 1 Vega mag (or 0.7 ± 0.5 AB mag), consistent with typical galaxy colors at this sensitivity level (Figures 30 and 31 in Ashby et al. 2013; Bisigello et al. 2023). The newly identified source S7, however, only has an upper limit on its [F356W]–[F444W] color. For comparison with S7, we show planet evolutionary curves from AMES-Cond (Baraffe et al. 2003) and BEX (Linder et al. 2019). For the BEX cooling curves, we consider two different radiative transfer models for the planetary atmosphere, HELIOS and the version of petitCODE with clouds (Linder et al. 2019). With only an upper limit to the brightness of this object at F356W, we cannot make a definitive statement about the nature of S7, but based on its brightness at F444W alone, its mass is at or below $1\ M_{\rm Jup}$. Note that there is no sign of the planet predicted by Janson et al. (2020) as our detection limit (19 mag or $\sim330\ M_{M_{\oplus}}$ in F444W) is higher than the one they had predicted for those observations (24 mag or $\sim66\ M_{M_{\oplus}}$ in F444W).

4.2. What About Fomalhaut b?

The expected position of Fomalhaut b at the time of the JWST observations depends on whether the object is in a bound or unbound orbit (Gáspár & Rieke 2020). The expected

offsets with respect to Fomalhaut are: $(\Delta\alpha, \Delta\delta) = (-9\!''\!377, 11\!''\!144)$ and $(-9\!''\!809, 11\!''\!665)$, for the bound and unbound orbits, respectively. The failure to detect any F356W or F444W emission at the predicted position(s) of Fomalhaut b rules out the presence of any object more massive than $\sim 1~M_{\mathrm{Jup}}$ and is consistent with the hypothesis that the object is a dispersing remnant of a collision between two planetesimals. The scattered light seen at shorter wavelengths by HST would be much fainter at NIRCam wavelengths due to lower stellar flux $(\propto \lambda^{-2})$ and the expected lower scattering cross sections. Janson et al. (2020) suggest that the disruption of a planetesimal in the tidal field of a $\sim 0.2~M_{\mathrm{Jup}}$ planet located at a semimajor axis of 117 au might be the cause of the observed collisional remnant. Such an object is below the sensitivity of the current observation.

4.3. Upper Limits on Scattered Light from the Debris Disk

We do not detect scattered light from the outer debris ring. Starting with the RDI-processed images (not ADI images, where the extended disk would self-subtract during the roll subtraction), we summed the flux within an ellipsoid annulus corresponding to the known ring location but did not find any emission above the background. Based on the azimuthal rms deviation between $30°$ bins, we find an upper limit on the disk emission of $\sim 17~\Delta$mag/arcsec^2 in both the F356W and F444W filters. This contrast is more than an order of magnitude less than the optical contrast detected by HST/ACS in combined F606W and F814W data $(\sim 20~\Delta$mag/arcsec^2; Kalas et al. 2005). While JWST/NIRCam has lower effective throughput than HST/ACS (partially negating the advantage in primary mirror size), the poorer contrast limit relative to HST is primarily a result of fainter stellar flux and lower scattering cross sections at the longer wavelengths. Typical interstellar grains have a factor of ~ 10 smaller albedo at NIRCam wavelengths than at HST wavelengths Draine (2003) although large $(a = 3\text{–}5~\mu$m), ice-dominated grains can have comparable visible and near-IR albedos around $3\text{–}4~\mu$m (McCabe et al. 2011; Tazaki et al. 2021).

Comparing the JWST upper limit against the integrated thermal emission for the dust ring $(L_{\mathrm{disk}}/L_\star = 5.4 \times 10^{-5}$; Acke et al. 2012), we place an upper limit on the dust albedo of < 0.6 at JWST wavelengths (3.56, 4.44 μm). While this rules out grains of pure ice, such dust has already been excluded by the much lower HST albedo measurement of $\sim 0.05\text{–}0.10$ at optical wavelengths.

5. Discussion

All of the objects in Table 3 with the exception of S7 have counterparts in deep Keck or HST imaging from earlier epochs. The incidence of background objects (almost exclusively galaxies at these wavelengths and sensitivity levels) can be assessed from a variety of references. Hutchings et al. (2002) suggest 10 objects per arcmin^2 down to $K_s = 20.5$ mag (Vega). Ashby et al. (2013, Figures 32 and 33) find cumulative source densities of 15 sources per arcmin^2 down to [IRAC2] = 19 (Vega mag) or 22.2 (AB mag) and 24 sources per arcmin^2 down to [IRAC1] = 20 (Vega mag) or 22.8 (AB mag). At longer wavelengths, Papovich et al. (2004) find a cumulative source density of ~ 8 per arcmin^2 down to the 60 μJy brightness of the MIRI GDC cloud at 23 μm. A rectangular region containing the entire MIRI disk is approximately

$40'' \times 20'' = 0.22$ arcmin^2, leading to an expected number of $3 \sim 5$ F444W sources compared to the ~ 7 seen here. The projected annular size of the outer ring itself is smaller, 0.06 arcmin^2, with an expectation of ~ 1 source within the outer ring.

Polletta et al. (2007) give template SEDs covering visible to far-IR wavelengths for 25 galaxy types, including ellipticals, spirals, AGN, and starburst systems.[15] These templates were derived using the GRASIL code fitted to data obtained between UV to far-IR wavelengths (Silva et al. 1998). Varying only the redshift and an amplitude scaling factor, we fitted photometric data from NIRCam, MIRI, Keck, and ALMA for S1. The Keck H-band brightness is 20.9 ± 0.3 Vega mag or $4.5 \pm 1~\mu$Jy (Kennedy et al. 2023). We estimate the ALMA 1.3 mm flux density as $5\times$ the 1σ noise level of 1.3 μJy = 6.5 μJy (MacGregor et al. 2017). The best-fitting SEDs correspond to active galaxies like Markarian 231, NGC6240, or the average Seyfert 2 (Figure 11). These luminous starburst galaxies have the large amounts of hot dust needed to be consistent with the observations, which is lacking in the more normal spiral and other galaxies in the SWIRE library. Starburst galaxies of this type are quite common at redshifts ~ 1 (Kartaltepe et al. 2012).

Late-type T or Y brown dwarfs at distances of a few hundred parsecs are an alternative contaminant. Comparing the [F356W] magnitudes and the [F356W]–[F444W] colors of S2 with IRAC Ch1 and Ch2 colors of nearby brown dwarfs suggests that S5 could be a mid-T dwarf at 120 pc (Luhman et al. 2007). Distant brown dwarf candidates have been found in the GLASS-JWST field (Nonino et al. 2023) and in the JADES field (Hainline et al. 2020) with multifilter SEDs well fitted by T/Y brown dwarf models. Twenty-one secure and possible brown dwarf candidates were identified in the medium and deep JADES footprint of 0.017 deg^2, or 0.33 objects per arcmin^2 for temperatures ranging from 400 to 1400 K. This result is consistent with theoretical expectations of 0.2–0.4 M8-T8 objects per arcmin^2 at $J < 30$ (AB mag; Ryan & Reid 2016) at a galactic latitude similar to Fomalhaut's $(b = -65°)$.

S7 has [F356W]–[F444W] > 0.7 (Vega Mag) which is relatively rare among field galaxies (Ashby et al. 2013, Figure 31) and lowers the probability that it is a background galaxy compared to the above numbers. At the same time, the lower limit of the color is plausible for a distant T dwarf but significantly bluer than for typical models for Jovian mass objects (Figure 10). But S7's color is only a limit and neither the background object nor the exoplanet explanation can be confirmed or rejected in the absence of the second astrometric epoch and improved photometry is now approved for Cycle 2 (PID#3925).

6. Conclusions

NIRCam coronagraphy was used to examine the regions around Fomalhaut in search of candidate planets that might explain the structure of the debris disk with its multiple rings. The observations achieved contrast levels of 10^{-7} outside of $1''$ corresponding to planet masses $\leqslant 1~M_{\mathrm{Jup}}$. Nine of the ten reliable detections correspond to objects seen in Keck or HST imaging from earlier epochs, ruling them out as exoplanet candidates. The object S7 is located within the inner dust ring seen in MIRI imaging and is detected only in F444W. It has no

---

[15] http://www.iasf-milano.inaf.it/~polletta/templates/swire_templates.html

obvious counterpart in earlier epochs and so might be a candidate planet subject to verification in future observations.

The source S1 is directly associated with the MIRI GDC object and has counterparts in NIRCam and earlier deep imaging. Its SED is similar to ultra-luminous IR galaxies like Arp 220. The other objects similarly have NIRCam colors consistent with background galaxies, or possibly in the case of S5, a distant brown dwarf. No NIRCam object is seen at the position of Fomalhaut b, consistent with its interpretation of a dissipating remnant of a collisional event.

It is important to note that outside of the speckle-dominated region, the sensitivity of these observations is limited by detector noise and the selected integration time. The approved JWST Cycle 2 program (PID # 3925) will have almost 4 (F444W) and 8 (F356W) times more integration time in full-frame imaging than this initial reconnaissance and will push the detection limit from $\sim$0.6 $M_{\rm Jup}$ down to $\sim$0.3–0.4 $M_{\rm Jup}$ at separations $\gtrsim$5″. In addition to confirming (or rejecting) S7 as being associated with Fomalhaut, the Cycle 2 program might identify one or more of the planets expected to exist on the basis of the complex disk structure discovered in the MIRI results (Gáspár et al. 2023).

Acknowledgments

Facility: JWST.

Software: astropy (Astropy Collaboration et al. 2013, 2018, 2022), jwst (Bushouse et al. 2023), NIRCoS (Kammerer et al. 2022), pyNRC (J. Leisenring 2023 in preparation), pyKLIP (Wang et al. 2015), species (Stolker et al. 2020), WebbPSF (Perrin et al. 2014), WebbPSF_ext (J. Leisenring 2023 in preparation).

Appendix
## pyKLIP Results of Forward Model Photometry and Astrometry

Figures 12, 13, and 14 show the output of pyKLIP's astrometry and photometry model fit. The comparison of the PSF-subtracted image versus the forward model, and its residuals, gives a visual representation of the the source extraction accuracy. The corner plots show how well the MCMC walkers converge to a solution. For S1 and S8 for instance, the MCMC iterations converge well given the S/Ns of these detections.

For completeness, we include the results of the model fits for sources 3, 4, and 5, in Figures 15, 16, 17. Although the photometry and astrometry of these sources were ultimately recovered with an aperture-photometry-based method, we report the MCMC model fit result figures to showcase the spurious uncertainties that stem from the low flux combined with the probable extended nature of these sources.

Filter F356W

Filter F444W
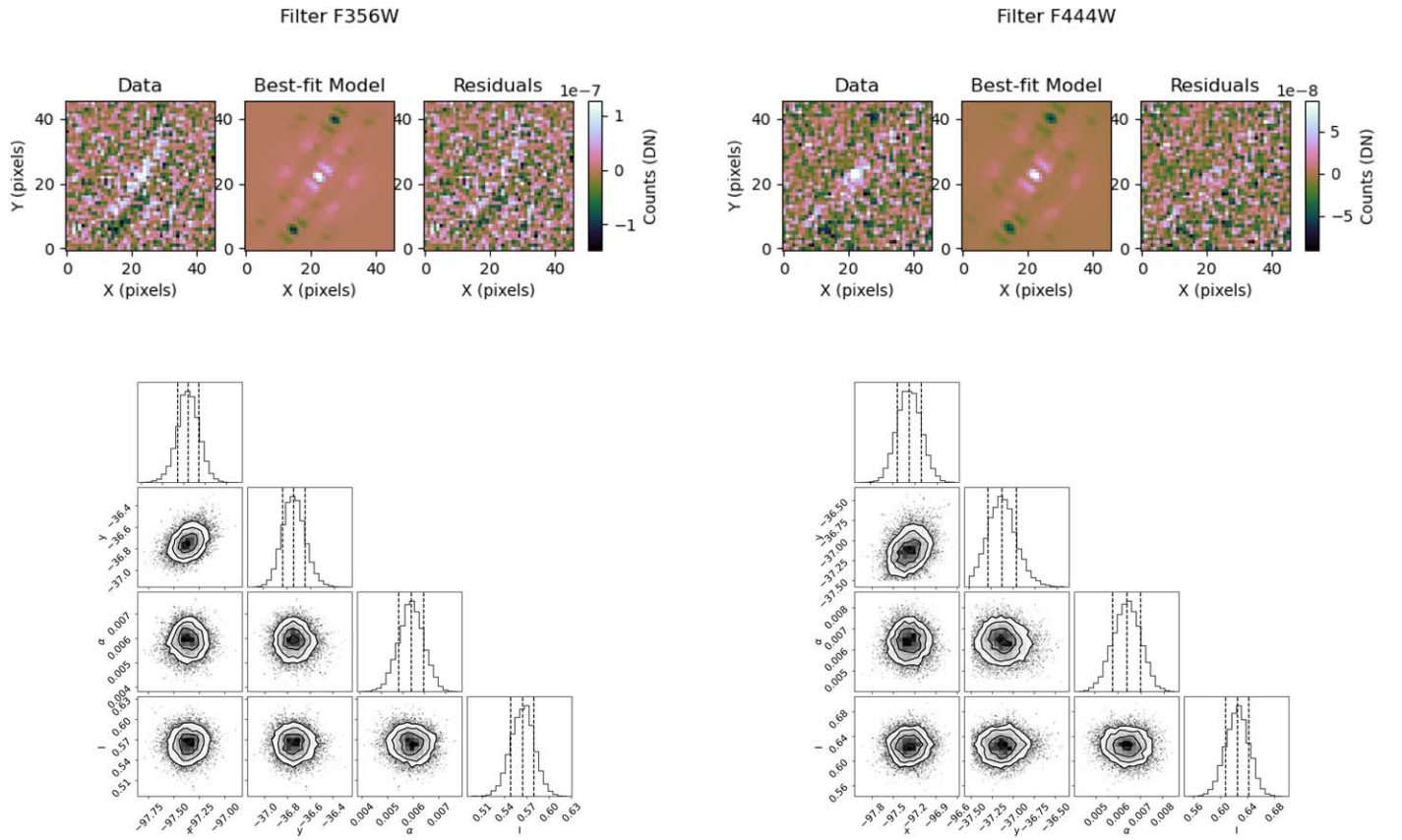
Figure 12. Top: Three-panel images showing data, model, and residuals for NIRCam S1 at F356W (left) and F444W (right). Bottom: The MCMC post-processing analysis gives the (*x*, y) position in pixels, the relative flux, and a correlation length, a Gaussian hyperparameter. This fit shows robust detections at both wavelengths. The same analysis is applied to all sources discussed in Table 3.
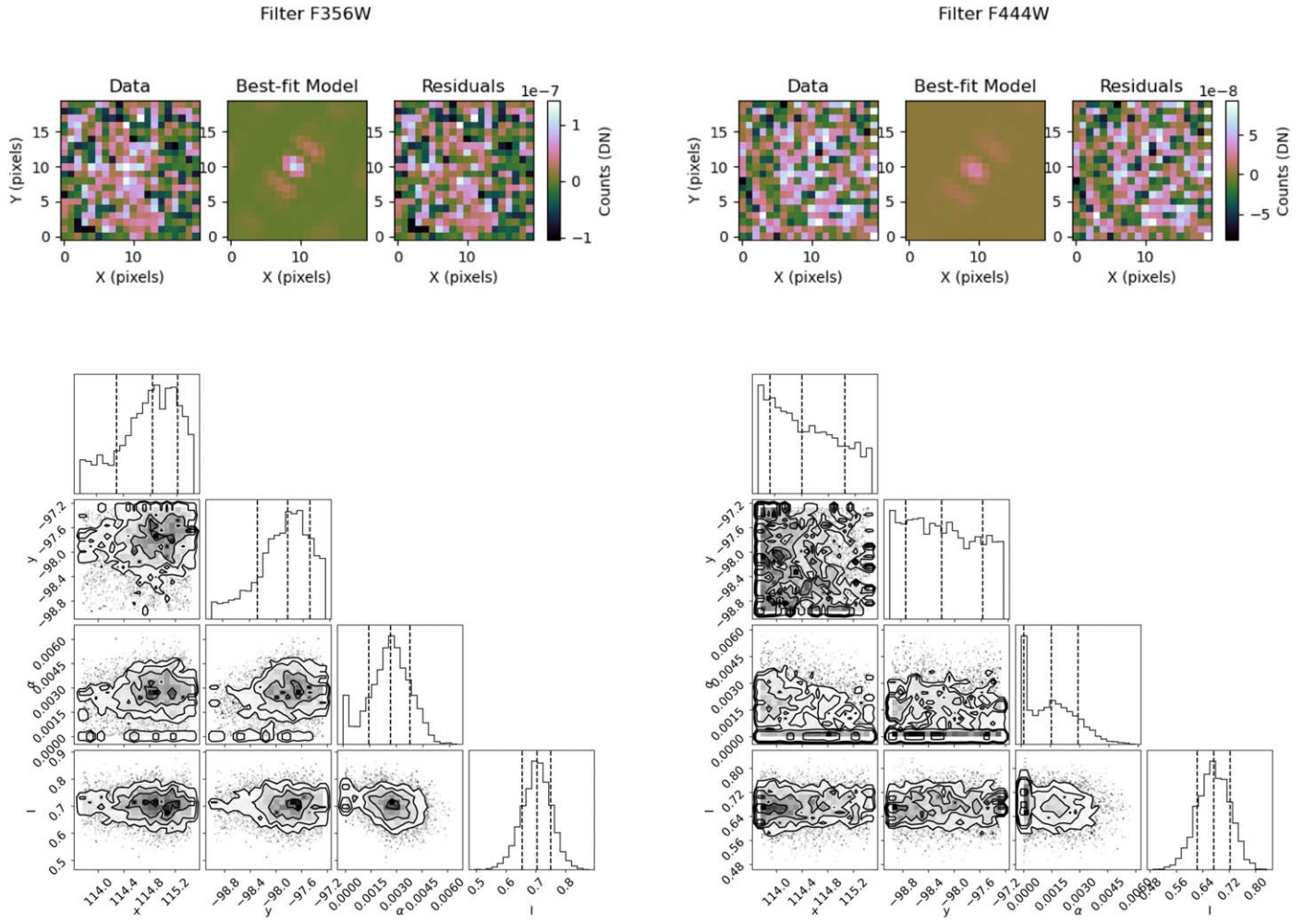
Figure 13. Same as Figure 12, but for *S2*.
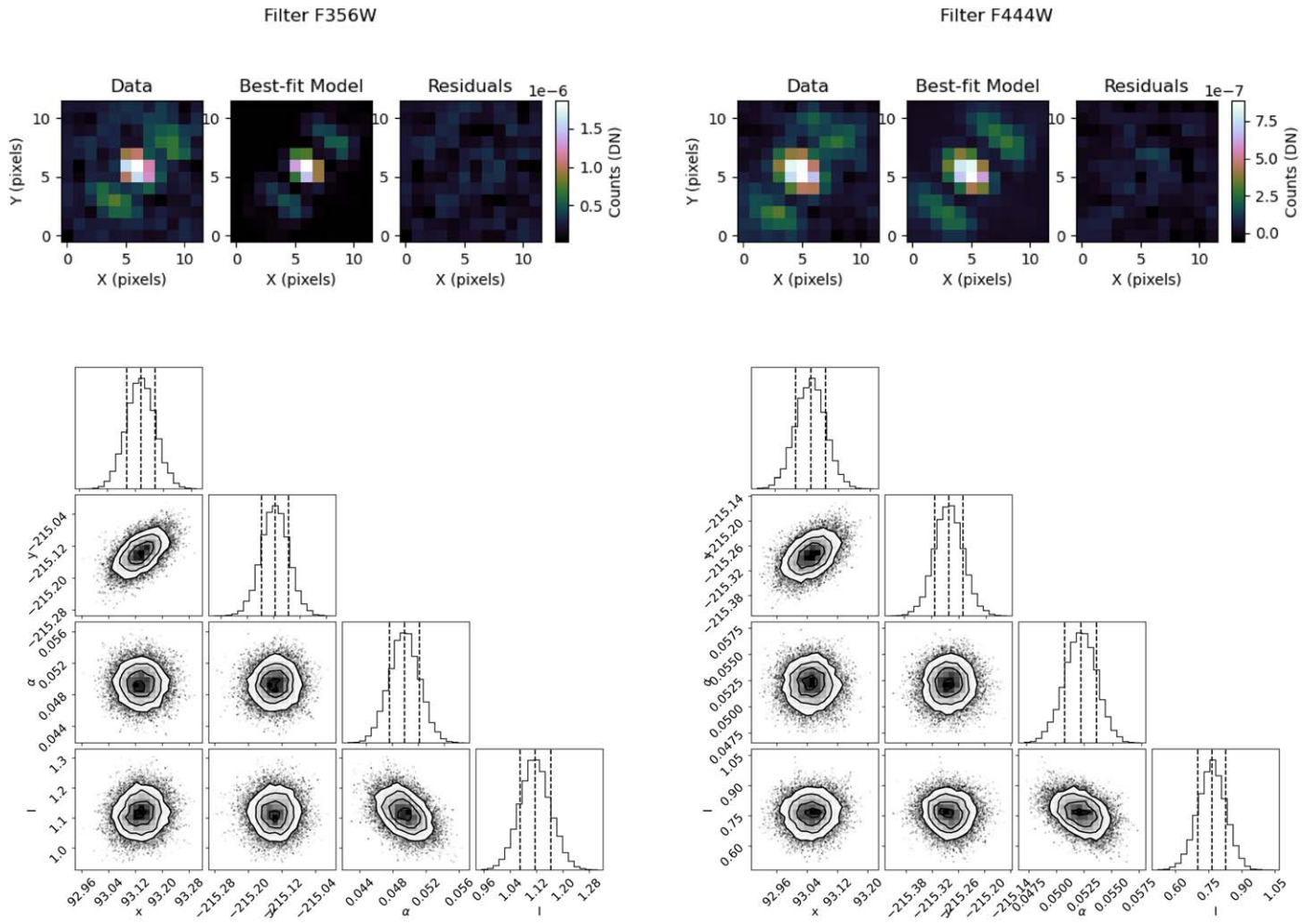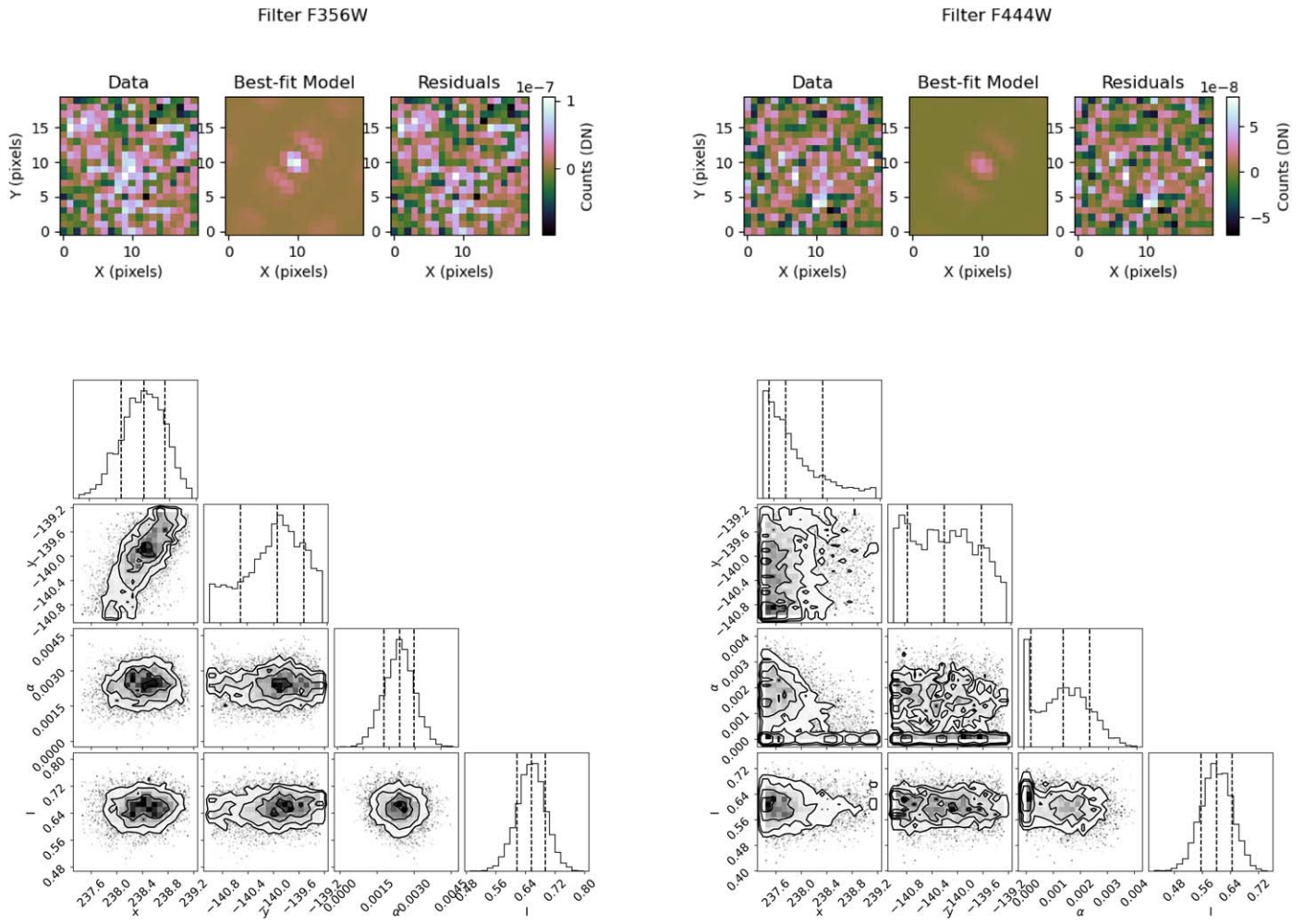
Figure 14. Same as Figure 12, but for source HST #1.

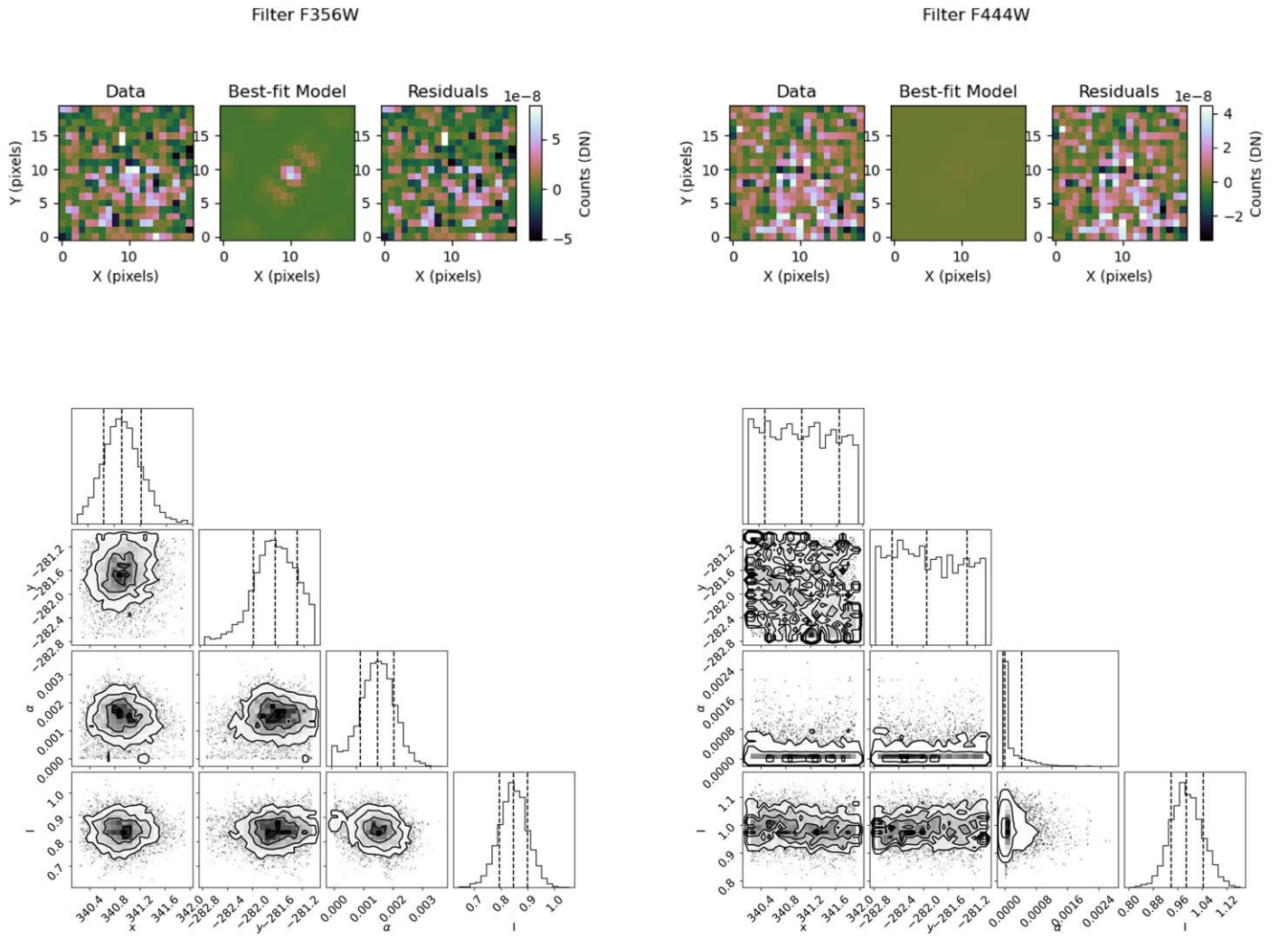**Figure 15.** Same as Figure 12, but for source 3.
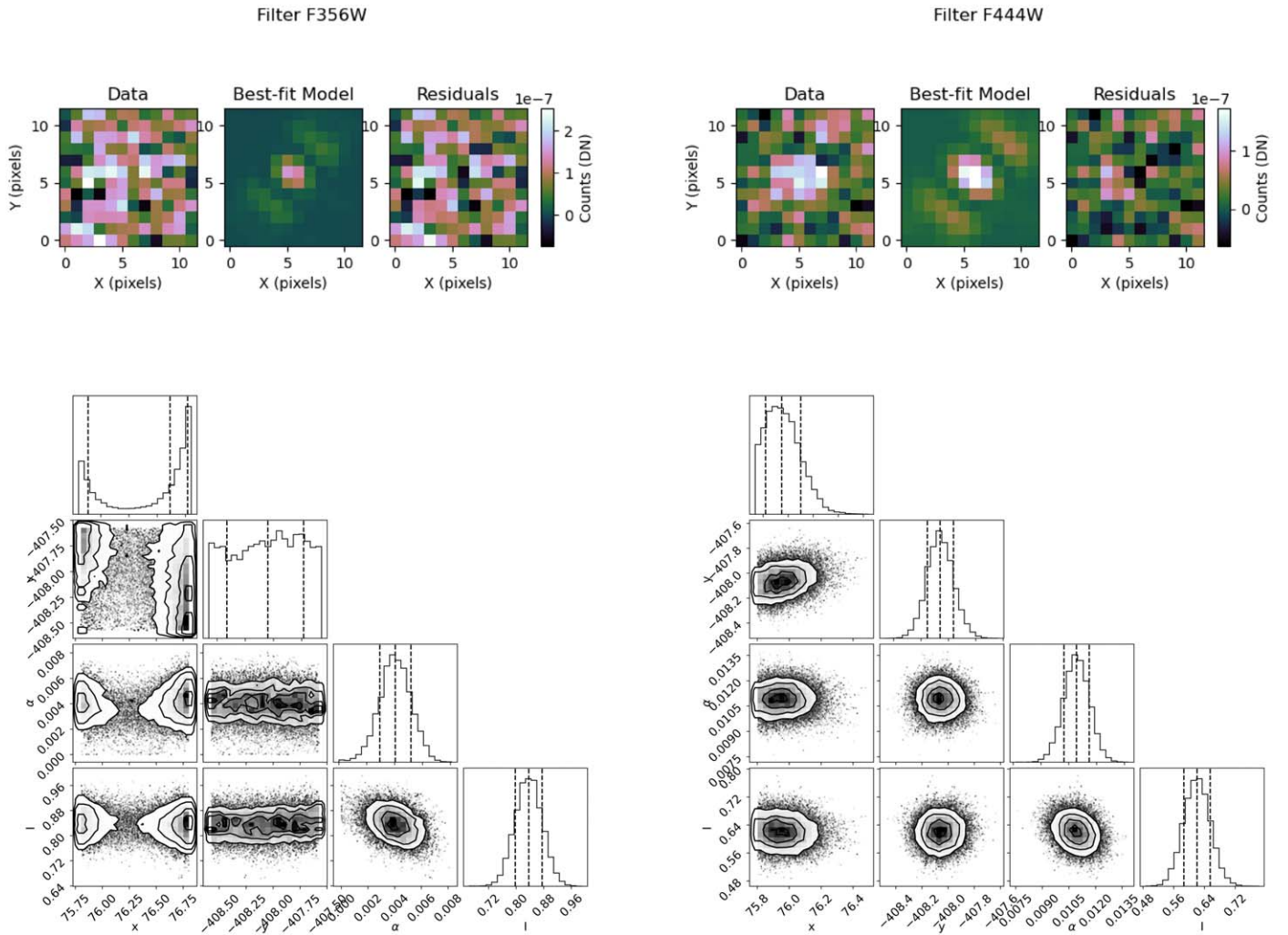
Figure 16. Same as Figure 12, but for source 4.

Filter F356W

Filter F444W

Figure 17. Same as Figure 12, but for source 5.

ORCID iDs

Marie Ygouf ⓘ https://orcid.org/0000-0001-7591-2731
Charles A. Beichman ⓘ https://orcid.org/0000-0002-5627-5471
Jorge Llop-Sayson ⓘ https://orcid.org/0000-0002-3414-784X
Geoffrey Bryden ⓘ https://orcid.org/0000-0001-5966-837X
Jarron M. Leisenring ⓘ https://orcid.org/0000-0002-0834-6140
András Gáspár ⓘ https://orcid.org/0000-0001-8612-3236
Marcia J. Rieke ⓘ https://orcid.org/0000-0002-7893-6170
George H. Rieke ⓘ https://orcid.org/0000-0003-2303-6519
Schuyler Grace Wolff ⓘ https://orcid.org/0000-0002-9977-8255
Thomas L. Roellig ⓘ https://orcid.org/0000-0002-6730-5410
Kate Su ⓘ https://orcid.org/0000-0002-3532-5580
Kevin N. Hainline ⓘ https://orcid.org/0000-0003-4565-8239
Klaus W. Hodapp ⓘ https://orcid.org/0000-0003-0786-2140
Thomas P. Greene ⓘ https://orcid.org/0000-0002-8963-8056
Michael R. Meyer ⓘ https://orcid.org/0000-0003-1227-3084
John Stansberry ⓘ https://orcid.org/0000-0003-2434-5225
Martha Boyer ⓘ https://orcid.org/0000-0003-4850-9589
Doug Johnstone ⓘ https://orcid.org/0000-0002-6773-459X
Scott Horner ⓘ https://orcid.org/0000-0001-9886-6934
Alexandra Z. Greenbaum ⓘ https://orcid.org/0000-0002-7162-8036

References

Absil, O., Mennesson, B., Le Bouquin, J.-B., et al. 2009, ApJ, 704, 150
Acke, B., Min, M., Dominik, C., et al. 2012, A&A, 540, A125
Amara, A., & Quanz, S. P. 2012, MNRAS, 427, 948
Ashby, M. L. N., Willner, S. P., Fazio, G. G., et al. 2013, ApJ, 769, 80
Astropy Collaboration, Price-Whelan, A. M., Lim, P. L., et al. 2022, ApJ, 935, 167
Astropy Collaboration, Price-Whelan, A. M., Sipőcz, B. M., et al. 2018, AJ, 156, 123
Astropy Collaboration, Robitaille, T. P., Tollerud, E. J., et al. 2013, A&A, 558, A33
Aumann, H. H. 1985, PASP, 97, 885
Baraffe, I., Chabrier, G., Barman, T. S., et al. 2003, A&A, 402, 701
Beust, H., Augereau, J.-C., Bonsor, A., et al. 2014, A&A, 561, A43
Bisigello, L., Gandolfi, G., Grazian, A., et al. 2023, A&A, 676, A76
Bohlin, R. C., Mészáros, S., Fleming, S. W., et al. 2017, AJ, 153, 234
Boley, A. C., Payne, M. J., Corder, S., et al. 2012, ApJL, 750, L21
Bushouse, H., Eisenhamer, J., Dencheva, N., et al. 2023, JWST Calibration Pipeline, Zenodo, doi:10.5281/ZENODO.10022973
Carpenter, J. M., Bouwman, J., Mamajek, E. E., et al. 2009, ApJS, 181, 197
Carter, A. L., Hinkley, S., Kammerer, J., et al. 2023, ApJL, 951, L20
Carter, B. S. 1990, MNRAS, 242, 1
Currie, T., Cloutier, R., Debes, J. H., et al. 2013, ApJL, 777, L6
Draine, B. T. 2003, ApJ, 598, 1017
Eiroa, C., Marshall, J. P., Mora, A., et al. 2013, A&A, 555, A11
Foreman-Mackey, D., Hogg, D. W., Lang, D., et al. 2013, PASP, 125, 306
Gáspár, A., & Rieke, G. 2020, PNAS, 117, 9712
Gáspár, A., Rieke, G. H., & Ballering, N. 2016, ApJ, 826, 171
Gáspár, A., Rieke, G. H., & Balog, Z. 2013, ApJ, 768, 25

Gáspár, A., Wolff, S. G., Rieke, G. H., et al. 2023, NatAs, 7, 790

Gillett, F. 1985, in Light on Dark Matter, Astrophysics and Space Library, ed. F. P. Israel, Vol. 124 (Dordrecht: Reidel Publishing), 61

Girard, J. H., Leisenring, J., Kammerer, J., et al. 2022, Proc. SPIE, 12180, 121803Q

Gray, R. O., Corbally, C. J., Garrison, R. F., et al. 2006, AJ, 132, 161

Greenbaum, A. Z., Llop-Sayson, J., Lew, B. W. P., et al. 2023, ApJ, 945, 126

Hainline, K. N., Hviding, R. E., Rieke, M., et al. 2020, ApJ, 892, 125

Holland, W. S., Greaves, J. S., Dent, W. R. F., et al. 2003, ApJ, 582, 1141

Hutchings, J. B., Stetson, P. B., Robin, A., et al. 2002, PASP, 114, 761

Janson, M., Quanz, S. P., Carson, J. C., et al. 2015, A&A, 574, A120

Janson, M., Wu, Y., Cataldi, G., et al. 2020, A&A, 640, A93

Kalas, P., Graham, J. R., Chiang, E., et al. 2008, Sci, 322, 1345

Kalas, P., Graham, J. R., & Clampin, M. 2005, Natur, 435, 1067

Kammerer, J., Girard, J., Carter, A. L., et al. 2022, Proc. SPIE, 12180, 121803N

Kartaltepe, J. S., Dickinson, M., Alexander, D. M., et al. 2012, ApJ, 757, 23

Kennedy, G. M., Lovell, J. B., Kalas, P., et al. 2023, MNRAS, 524, 2698

Kenworthy, M. A., Meshkat, T., Quanz, S. P., et al. 2013, ApJ, 764, 7

Krist, J. E., Balasubramanian, K., Muller, R. E., et al. 2010, Proc. SPIE, 7731, 77313J

Lajoie, C.-P., Soummer, R., Pueyo, L., et al. 2016, Proc. SPIE, 9904, 99045K

Lawler, S. M., Greenstreet, S., & Gladman, B. 2015, ApJL, 802, L20

Linder, E. F., Mordasini, C., Mollière, P., et al. 2019, A&A, 623, A85

Luhman, K. L., Patten, B. M., Marengo, M., et al. 2007, ApJ, 654, 570

MacGregor, M. A., Matrà, L., Kalas, P., et al. 2017, ApJ, 842, 8

Mamajek, E. E. 2012, ApJL, 754, L20

Marengo, M., Stapelfeldt, K., Werner, M. W., et al. 2009, ApJ, 700, 1647

Marley, M. S., Saumon, D., Visscher, C., et al. 2021, ApJ, 920, 85

Mawet, D., Milli, J., Wahhaj, Z., et al. 2014, ApJ, 792, 97

McCabe, C., Duchêne, G., Pinte, C., et al. 2011, ApJ, 727, 90

Mermilliod, J.-C., & Mermilliod, M. 1994, Catalogue of Mean UBV Data on Stars (New York: Springer-Verlag)

Nielsen, E. L., De Rosa, R. J., MacIntosh, B., et al. 2019, AJ, 158, 13

Nonino, M., Glazebrook, K., Burgasser, A. J., et al. 2023, ApJL, 942, L29

Papovich, C., Dole, H., Egami, E., et al. 2004, ApJS, 154, 70

Perrin, M. D., Pueyo, L., Van Gorkom, K., et al. 2018, Proc. SPIE, 10698, 1069809

Perrin, M. D., Sivaramakrishnan, A., Lajoie, C.-P., et al. 2014, Proc. SPIE, 9143, 91433X

Polletta, M., Tajer, M., Maraschi, L., et al. 2007, ApJ, 663, 81

Pueyo, L. 2016, ApJ, 824, 117

Rieke, G. H., Su, K. Y. L., Stansberry, J. A., et al. 2005, ApJ, 620, 1010

Rieke, M. J., Kelly, D. M., Misselt, K., et al. 2023, PASP, 135, 028001

Ruffio, J.-B., Macintosh, B., Wang, J. J., et al. 2017, ApJ, 842, 14

Ryan, R. E., & Reid, I. N. 2016, AJ, 151, 92

Sierchio, J. M., Rieke, G. H., Su, K. Y. L., & Gáspár, A. 2014, ApJ, 785, 33

Silva, L., Granato, G. L., Bressan, A., et al. 1998, ApJ, 509, 103

Soummer, R., Pueyo, L., & Larkin, J. 2012, ApJL, 755, L28

Stapelfeldt, K. R., Holmes, E. K., Chen, C., et al. 2004, ApJS, 154, 458

Stolker, T., Quanz, S. P., Todorov, K. O., et al. 2020, A&A, 635, A182

Su, K. Y. L., Rieke, G. H., Defrére, D., et al. 2016, ApJ, 818, 45

Su, K. Y. L., Rieke, G. H., Malhotra, R., et al. 2013, ApJ, 763, 118

Su, K. Y. L., Rieke, G. H., Stansberry, J. A., et al. 2006, ApJ, 653, 675

Tazaki, R., Murakawa, K., Muto, T., et al. 2021, ApJ, 921, 173

Thureau, N. D., Greaves, J. S., Matthews, B. C., et al. 2014, MNRAS, 445, 2558

van Leeuwen, F. 2007, A&A, 474, 653

Wang, J. J., Ruffio, J.-B., De Rosa, R. J., et al., 2015 pyKLIP: PSF Subtraction for Exoplanets and Disks, Astrophysics Source Code Library, ascl:1506.001

White, J. A., Boley, A. C., Dent, W. R. F., Ford, E. B., & Corder, S. 2017, MNRAS, 466, 4201

Wright, G. S., Rieke, G. H., Glasse, A., et al. 2023, PASP, 135, 1046

Wyatt, M. C. 2008, ARA&A, 46, 339